

5. SITE 1077¹

Shipboard Scientific Party²

HOLE 1077A

Position: 5°10.7969'S, 10°26.1960'E
Start hole: 0530 hr, 29 August 1997
End hole: 1130 hr, 30 August 1977
Time on hole: 30.00 hr
Seafloor (drill pipe measurement from rig floor, mbrf): 2391.5
Total depth (drill pipe measurement from rig floor, mbrf): 2596
Distance between rig floor and sea level (m): 11.5
Water depth (drill pipe measurement from sea level, m): 2380
Penetration (mbsf): 204.5
Coring totals:
Type: APC
Number: 22
Cored: 204.5 m
Recovered: 208.99 m (102.20%)
Lithology:
Unit I: diatom-rich, diatom-bearing, nannofossil-bearing, and nanno-fossil-rich clay

HOLE 1077B

Position: 5°10.7977'S, 10°26.1831'E
Start hole: 1130 hr, 30 August 1997
End hole: 0455 hr, 31 August 1977
Time on hole: 17.42 hr
Seafloor (drill pipe measurement from rig floor, mbrf): 2392.9
Total depth (drill pipe measurement from rig floor, mbrf): 2598
Distance between rig floor and sea level (m): 11.5
Water depth (drill pipe measurement from sea level, m): 2381.4
Penetration (mbsf): 205.1
Coring totals:
Type: APC
Number: 22
Cored: 205.1 m
Recovered: 211.53 m (103.14%)
Lithology:
Unit I: diatom-rich, diatom-bearing, nannofossil-bearing, and nanno-fossil-rich clay

HOLE 1077C

Position: 5°10.7995'S, 10°26.1687'E
Start hole: 0455 hr, 31 August 1997
End hole: 1206 hr, 31 August 1977
Time on hole: 7.18 hr
Seafloor (drill pipe measurement from rig floor, mbrf): 2396.7
Total depth (drill pipe measurement from rig floor, mbrf): 2419.5
Distance between rig floor and sea level (m): 11.5
Water depth (drill pipe measurement from sea level, m): 2385.2
Penetration (mbsf): 22.8
Coring totals:
Type: APC
Number: 3
Cored: 22.8 m
Recovered: 16.46 m (72.19%)
Lithology:
Unit I: diatom-rich, diatom-bearing, nannofossil-bearing, and nanno-fossil-rich clay

Principal results: Site 1077 is the intermediate-water drill site on a depth transect in the Lower Congo Basin. It is located in 2382-m deep water in a complex environment dominated by (1) freshwater input from the Congo River, (2) seasonal coastal upwelling and associated filaments and eddies moving offshore, and (3) incursions of open-ocean waters, especially from the South Equatorial Countercurrent. We expect a close tie-in of climatic records from the continent and the ocean in this area. In the fan-margin deposits, the intercalation of pelagic and terrigenous information provides an excellent opportunity for studying cross-correlations of climatic effects on land and at sea. Site 1077, in connection with Sites 1075 and 1076 in the Lower Congo Basin, will allow us to reconstruct the changing influence of Congo River, coastal upwelling, and open-ocean contributions to the dynamics of the region.

Three holes were cored with the advanced hydraulic piston corer (APC) at Site 1077 to a maximum depth of 205.1 meters below seafloor (mbsf), which recovered an apparently continuous hemipelagic sedimentary section spanning the entire Pleistocene (1.77–0 Ma). Drilling at Hole 1077A recovered 22 APC cores to a total depth of 204.5 mbsf, Hole 1077B was cored with the APC to 205.1 mbsf, and three APC cores were taken at Hole 1077C to a total depth of 22.8 mbsf.

Sediments form one lithostratigraphic unit comprised of intercalated, 40- to 150-cm-thick intervals of greenish gray diatom-rich, diatom-bearing, nannofossil-bearing, and nannofossil-rich clay. The relative abundances of the biogenic components vary greatly with depth. Most of the sediment apparently is strongly bioturbated. Pteropod shells and small shell fragments are present in many intervals. Rare, friable nodules, possibly phosphatic, are interspersed throughout the sediment. The calcium carbonate content varies between 0.8 and 13.2 wt%. The biogenic fraction contains rare to frequent diatoms, rare nannofossils, silicoflagellates, siliceous sponge spicules, phytoliths, and traces of radiolarian and foraminifer fragments. Authigenic components are dominated by the presence of glauconite, dolo-

¹Wefer, G., Berger, W.H., Richter, C., et al., 1998. *Proc. ODP, Init. Repts.*, 175: College Station, TX (Ocean Drilling Program).

²Shipboard Scientific Party is given in the list preceding the Table of Contents.

mite, and iron sulfides. X-ray diffraction (XRD) analysis shows that the clastic fraction is dominated by smectite, kaolinite/illite, quartz, and minor amounts of albitic feldspar.

Detailed comparisons between the magnetic susceptibility record generated on the multisensor track (MST) and high-resolution color reflectance measured with the Minolta spectrophotometer demonstrated complete recovery of the sedimentary sequence down to 183 meters composite depth (mcd), with gaps in the continuous record at 25 and 125 mcd.

Calcareous microfossil abundance and preservation varies between the different groups and deteriorates with depth. Benthic foraminifers are abundant and well preserved down to 120 mbsf, calcareous nanofossils down to 130 mbsf, and planktonic foraminifers down to 150 mbsf. Siliceous microfossils are abundant and well preserved throughout the entire section. Both planktonic and benthic foraminiferal assemblages display a major change at 52 mbsf, which may represent a change in position of water masses at this location.

A magnetostratigraphy was determined after alternating-field (AF) demagnetization at 20 mT. The Matuyama/Brunhes boundary occurs at ~120 mbsf, and the termination and onset of the Jaramillo Subchron (C1r.1n) was identified in the lower part of the section at ~130 and 140 mbsf, respectively.

Sediments average 2.3 wt% total organic carbon (TOC), which is rather high for ocean margin areas and reflects a history of elevated primary production in this area. Interstitial water chemistry studies document a sequence of diagenetic processes caused largely by the degradation of organic matter and carbonate dissolution-precipitation reactions. Among these are moderately high levels of methane and carbon dioxide generated by in situ microbial activity. These postdepositional processes are strongly similar to those found at nearby Sites 1075 and 1076 on the Congo Margin. A high-resolution study of interstitial water and headspace methane was conducted over the depth range at which a prominent seismic reflector exists to test whether this reflector is caused by methane hydrate. None of the profiles of salinity, dissolved chloride, or methane are characteristic of hydrate presence. There is no chemical evidence of the presence of methane hydrate in any portion of the sequence recovered from Site 1077.

Physical sediment properties were determined both by high-resolution MST core logging and index properties measurements. Magnetic susceptibility and gamma-ray attenuation porosity evaluator (GRAPE) signals reveal pronounced cyclicities, which were used for high-quality stratigraphic correlation in conjunction with digital color data.

Hole 1077A was logged with a limited suite of sensors to test for the presence of gas hydrate as a potential cause of pronounced changes in seismic reflectivity between 80 and 120 mbsf, to provide data for core-log integration, and to obtain a continuous record as a proxy for paleoclimatic changes. The tool string included the natural gamma spectroscopy tool (NGT), long-spaced sonic (LSS), phasor dual-induction-spherically focused resistivity (DITE-SFL), and Lamont-Doherty high-resolution temperature (LDEO-TLT) sondes. The hole was logged from 202 to 74 mbsf. The recorded data are of good quality, although density variations were within the resolution of the sensors and the sonic tool measured very low in situ velocities between 1470 and 1510 m/s. No anomalous data indicating hydrate accumulations were found at the reflector depths. The natural gamma-ray profile correlates with core measurements and is a valuable indicator of coring-induced deformation. The gamma-ray profile is correlated to the changing clay content of the sediment and clearly follows the glacial/interglacial stages of the oxygen-isotope record. Preliminary spectral analysis of the tuned natural gamma-ray data shows a dominance of both the eccentricity and obliquity orbital cycles with a well-identified precessional signal.

On the whole, results for Site 1077 are similar to those for Site 1075, although sedimentation rates are higher. The shallower water depth at Site 1077 accounts for better preservation of calcareous fossils, especially in the upper portion of the sequence, where even pteropods (aragonite) were found in places. In combination with the high-resolution continuous 2-

m.y. record of Site 1075, Site 1077 should greatly contribute to our understanding of the changing conditions of sedimentation in this area. Depositional patterns will reflect climatically driven changes in the supply of riverine materials (Congo), upwelling export (seasonal coastal upwelling), and open-ocean contributions. The Milankovitch-related cyclicality of the changes is evident from inspection of a number of records, even at this preliminary stage of analysis.

BACKGROUND AND OBJECTIVES

For a discussion of the background and objectives for Site 1077, see "Background and Objectives" section, "Site 1075" chapter (this volume).

OPERATIONS

Hole 1077A (Proposed Site LCB-3A)

The 40-nmi voyage from Site 1076 to Site 1077 was accomplished at an average speed of 12.5 kt. As the vessel slowly approached the location using Global Positioning System coordinates, the beacon was deployed at 0534 hr on 29 August. Following an unsuccessful attempt at a mudline core from 2385.0 meters below rig floor (mbrf), the bit was positioned at 2387.0 mbrf, where Hole 1077A was spudded at 1210 hr on 29 August. The seafloor depth was established at 2380 (mbsl) by drill-pipe measurement (DPM). Advanced hydraulic piston corer (APC) Cores 175-1077A-1H through 22H were taken from 0 to 204.5 meters below seafloor (mbsf; Table 1; also see the expanded coring summary table on CD-ROM, back pocket, this volume), with 204.5 m cored and 209.5 m recovered (102.2% recovery). Cores were oriented starting with Core 4H. The Adara heat-flow shoe was deployed at Cores 5H (43.0 mbsf), 7H (62.0 mbsf), 10H (90.5 mbsf), and 13H (119.0 mbsf). Headspace analysis of the cores indicates the presence of biogenic methane with insignificant amounts of ethane (<10 ppm) and no discernible amounts of heavier hydrocarbons. The methane concentration peaked at 57 mbsf (54,717 ppm) and gradually tapered off with depth with another peak at 152 mbsf (44,860 ppm). Although some of the core exuded a mild sulfurous smell, concentrations of hydrogen sulfide were always <1 ppm and could not be measured.

Logging in Hole 1077A

Hole 1077A was logged with a limited suite of sensors to identify and locate the presence of gas hydrate in the sediments and to provide data for core-log integration. After a "go-devil" was pumped down the pipe to ensure the proper operation of the lockable float valve, the drill pipe was tripped to 63.5 mbsf, the top drive was picked up, and the bit was placed at 79.0 mbsf. The logging tool included the spectral gamma-ray, long-spacing sonic, phasor dual-induction, and the Lamont-Doherty high-resolution temperature Sondes and was deployed at 0725 hr on 30 August. The tool logged Hole 1077A at 400 m/hr from 202 to 79 mbsf. By 1115 hr on 30 August, the logging equipment was rigged down, and the top drive was set back as the drill string was pulled to the surface. The bit cleared the seafloor at 1130 hr on 30 August, ending operations at Hole 1077A.

Hole 1077B

The vessel was offset 20 m to the west, and Hole 1077B was spudded at 1235 hr on 30 August. The seafloor depth was established at 2381.4 meters below sea level (mbsl) by drill-pipe measurement (DPM). APC Cores 175-1077B-1H through 22H were taken from 0

Table 1. Coring summary for Site 1077.

Core	Date (Aug 1997)	Time (UTC)	Interval (mbsf)	Length cored (m)	Length recovered (m)	Recovery (%)
175-1077A-						
1H	29	1220	0.0-5.0	5.0	4.98	99.6
2H	29	1300	5.0-14.5	9.5	5.83	61.4
3H	29	1340	14.5-24.0	9.5	9.64	101.5
4H	29	1420	24.0-33.5	9.5	9.90	104.2
5H	29	1525	33.5-43.0	9.5	9.94	104.6
6H	29	1605	43.0-52.5	9.5	9.98	105.1
7H	29	1650	52.5-62.0	9.5	10.06	105.9
8H	29	1735	62.0-71.5	9.5	10.21	107.5
9H	29	1815	71.5-81.0	9.5	9.36	98.5
10H	29	1915	81.0-90.5	9.5	10.03	105.6
11H	29	2000	90.5-100.0	9.5	10.00	105.3
12H	29	2045	100.0-109.5	9.5	10.19	107.3
13H	29	2145	109.5-119.0	9.5	10.02	105.5
14H	29	2230	119.0-128.5	9.5	8.40	88.4
15H	29	2315	128.5-138.0	9.5	10.22	107.6
16H	30	0010	138.0-147.5	9.5	10.33	108.7
17H	30	0050	147.5-157.0	9.5	10.10	106.3
18H	30	0135	157.0-166.5	9.5	9.78	102.9
19H	30	0210	166.5-176.0	9.5	9.94	104.6
20H	30	0250	176.0-185.5	9.5	9.98	105.1
21H	30	0330	185.5-195.0	9.5	10.04	105.7
22H	30	0415	195.0-204.5	9.5	10.06	105.9
Coring totals:				204.5	208.99	102.2
175-1077B-						
1H	30	1245	0.0-5.6	5.6	5.62	100.4
2H	30	1325	5.6-15.1	9.5	8.60	90.5
3H	30	1400	15.1-24.6	9.5	9.36	98.5
4H	30	1445	24.6-34.1	9.5	9.66	101.7
5H	30	1525	34.1-43.6	9.5	9.45	99.5
6H	30	1610	43.6-53.1	9.5	9.93	104.5
7H	30	1715	53.1-62.6	9.5	9.78	102.9
8H	30	1800	62.6-72.1	9.5	10.02	105.5
9H	30	1845	72.1-81.6	9.5	9.91	104.3
10H	30	1930	81.6-91.1	9.5	10.16	106.9
11H	30	2010	91.1-100.6	9.5	10.08	106.1
12H	30	2050	100.6-110.1	9.5	9.81	103.3
13H	30	2125	110.1-119.6	9.5	10.73	112.9
14H	30	2210	119.6-129.1	9.5	9.05	95.3
15H	30	2250	129.1-138.6	9.5	9.34	98.3
16H	30	2330	138.6-148.1	9.5	9.82	103.4
17H	31	0020	148.1-157.6	9.5	10.06	105.9
18H	31	0105	157.6-167.1	9.5	10.34	108.8
19H	31	0150	167.1-176.6	9.5	9.93	104.5
20H	31	0235	176.6-186.1	9.5	9.87	103.9
21H	31	0310	186.1-195.6	9.5	10.06	105.9
22H	31	0350	195.6-205.1	9.5	9.95	104.7
Coring totals:				205.1	211.53	103.1
175-1077C-						
1H	31	0610	0.0-3.8	3.8	3.81	100.3
2H	31	0640	3.8-13.3	9.5	3.74	39.4
3H	31	0710	13.3-22.8	9.5	8.91	93.8
Coring totals:				22.8	16.46	72.2

Notes: UTC = Universal Time Coordinated. An expanded version of this coring summary table that includes lengths and depths of sections and comments on sampling is included on CD-ROM (back pocket, this volume).

to 205.1 mbsf (Table 1), with 205.1 m cored and 212.7 m recovered (103.6% recovery). The drill string was pulled back with the bit clearing the seafloor at 0455 hr on 31 August, thereby ending operations at Hole 1077B.

Hole 1077C

The vessel was offset 20 m to the west, and Hole 1077C was spudded with the APC at 0550 hr on 31 August. The seafloor depth was estimated from recovery to be at 2385.2 mbsl. Three APC cores were taken to a depth of 22.8 mbsf when operating time on site expired. Core recovery was only 72.2% of the cored interval because of the loss of watery sediments during the core retrieval process. The drill string was pulled out of the hole and cleared the seafloor at 0720 hr on 31 August, thereby ending operations at Site 1077. By 1206 hr on

31 August, the drilling equipment was secured and the vessel was under way to Lobito, Angola, for a scheduled arrival at 0700 hr on 2 September to take the Angolan scientific observer on board.

SITE GEOPHYSICS

For a discussion of site geophysics at Site 1077, see "Site Geophysics" section, "Site 1075" chapter (this volume).

LITHOSTRATIGRAPHY

Introduction

Three holes with a maximum penetration of 205.1 mbsf were drilled at Site 1077. Core disturbances occurred at the top of the first five cores. The upper 30 cm of these cores were disturbed and soupy and thus unsuitable for sampling. The first four cores in all three holes had a strong hydrogen sulfide smell indicating the microbial reduction of sulfate to sulfide.

Description of Lithostratigraphic Unit

The lithostratigraphic description for the sedimentary sequence from Site 1077 is based on data from the following sources: (1) visual core description, (2) smear-slide examination, (3) color reflectance measurements, (4) bulk calcium carbonate measurements, and (5) XRD measurements.

Sediments from Site 1077 form one lithostratigraphic unit composed of intercalated, 40- to 150-cm-thick intervals of olive-gray (5Y 3/2) and greenish gray (5GY 5/1) diatom-rich, diatom-bearing, nanofossil-bearing, and nanofossil-rich clay (Fig. 1). The relative abundances of the biogenic components varied greatly downcore. Color changes occur gradually over 20 to 30 cm except in Core 175-1077A-13H, where very abrupt color changes are observed. Variations in color between these intervals may be a result of fluctuations in contents of organic carbon, diatoms, and diagenetic conditions (see "Synthesis of Smear-Slide Analyses" section, this chapter). Greenish gray intervals become thicker and more abundant down each hole. Most of the sediment is moderately bioturbated. Bioturbation is most clearly seen in mottled intervals of 15- to 30-cm thickness that are associated with a pronounced change in sediment color (Fig. 2). Burrows range in diameter from 1 to 2 cm. Teropod shells are common in the first core from all three holes. Small shell fragments are present in many intervals throughout the sediment recovered from this site. The sediment progressively becomes more friable downcore as a result of compaction. Many cores contain gas expansion voids that were produced by the release of carbon dioxide and methane trapped in the sediment (see "Organic Geochemistry" section, this chapter). Rare, friable nodules are disseminated throughout certain intervals. Nodules may be phosphatic and range in diameter from 1 to 2 mm.

In Hole 1077A, calcium carbonate contents in sediments vary between 0.8 and 13.2 wt% (Fig. 1). Close sampling across a sharp color transition from greenish gray clay to olive-gray clay revealed that concentrations of CaCO₃, organic carbon, and total sulfur sharply increase in the olive-gray layer. Figure 1 shows that sediments below 120 mbsf have, on average, lower concentrations of CaCO₃ compared with sediments above 120 mbsf.

Synthesis of Smear-Slide Analyses

Smear-slide analyses indicate that the clastic component is dominated by clay minerals and minor amounts of quartz and feldspar. The biogenic portions of sediments contain rare to frequent diatoms, rare

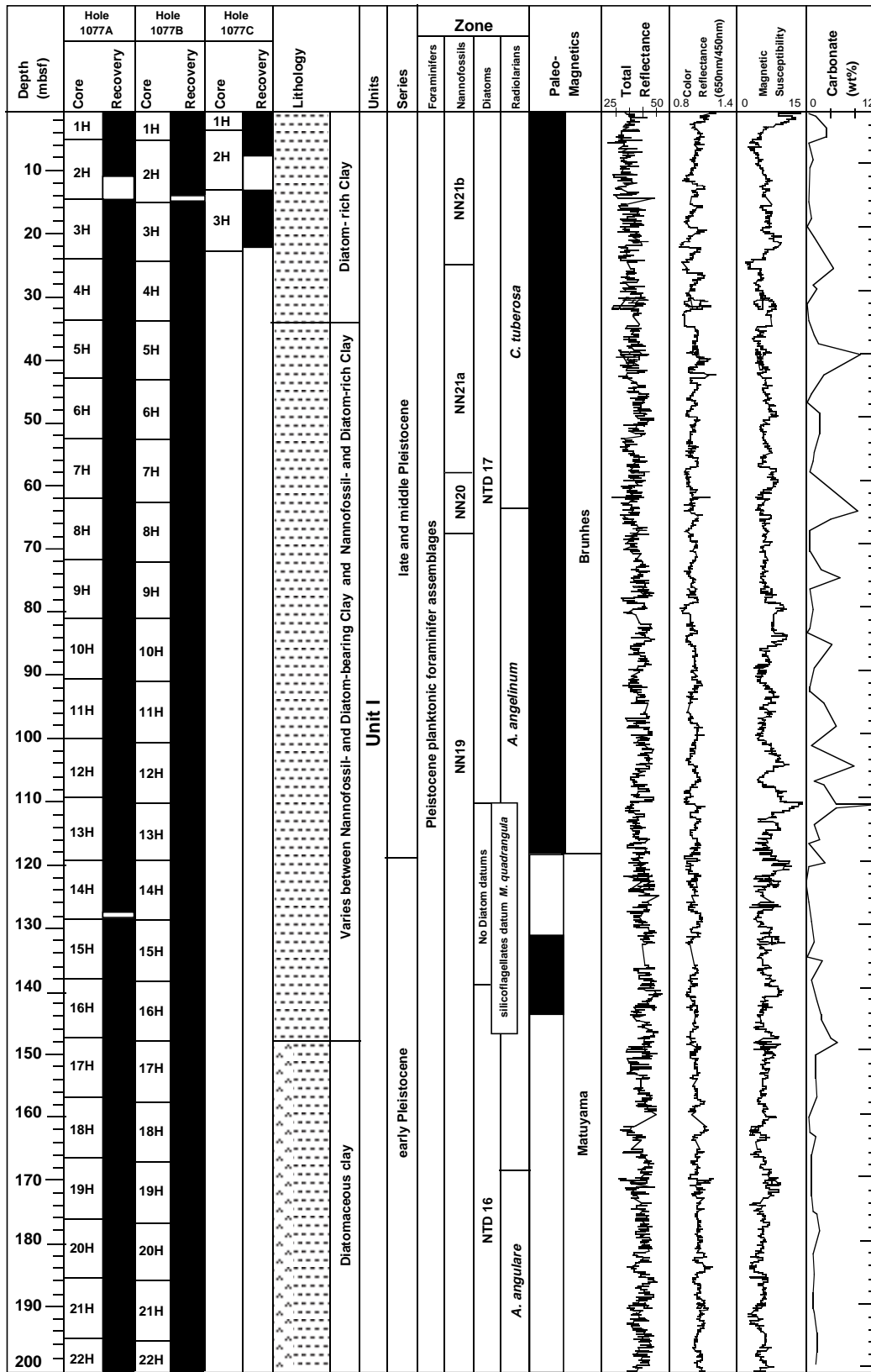


Figure 1. Composite stratigraphic section for Site 1077 showing core recovery in all holes, a simplified summary of lithology, age, total reflectance (400–700 nm), color reflectance (650 nm/450 nm), magnetic susceptibility, and calcium carbonate content.

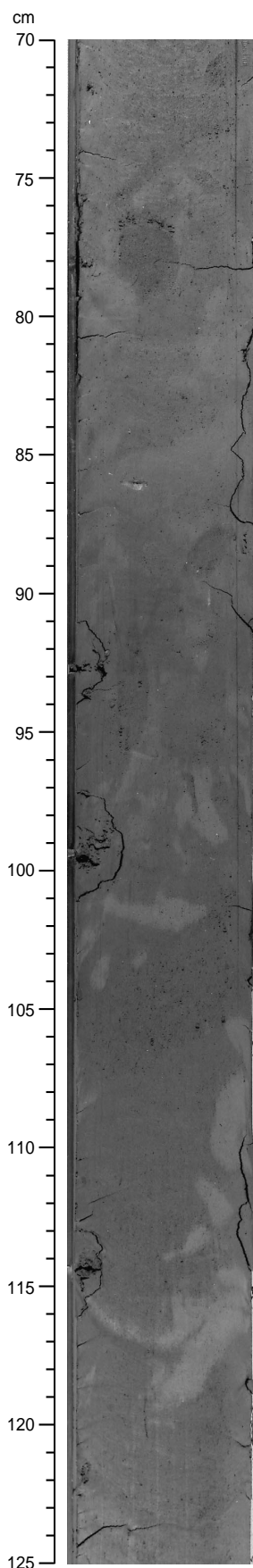


Figure 2. Photograph of bioturbated interval 175-1077A-6H-5, 70–125 cm. Bioturbation is apparent in this interval because of the mixing of olive-gray and greenish diatom-rich clay.

nannofossils, silicoflagellates, siliceous sponge spicules, phyloliths, and traces of radiolarian and foraminifer fragments. Variations in the abundances of diatoms are not directly related to color changes from greenish gray to olive-gray intervals.

Authigenic components are dominated by the presence of glauconite, dolomite, and iron sulfides. Worm casts, diatom frustules, radiolarians, and glauconite peloids often contain pyrite. Small dolomite rhombohedrons (6–100 μm) are found at all depths in the three holes. Iron sulfides are present primarily in the form of disseminated pyrite and framboidal pyrite, confirming the process of bacterial sulfate reduction. Framboidal pyrite is commonly observed in diatom tests. Euhedral pyrite crystals frequently replace glauconite peloids. In general, olive-gray (5Y 3/2) intervals contain more framboidal pyrite relative to glauconite than that found in the greenish gray (5GY 5/1) intervals.

X-ray Diffraction Analysis

XRD analysis of the sediments from Hole 1077A reveals that the clastic fraction is dominated by smectite, kaolinite/illite, and quartz. Pyrite is also present as an accessory mineral in all samples. Glauconite is not observed; it is probably masked in the X-ray patterns by other clay minerals. The smectites are generally poorly crystallized. Shipboard XRD spectra for Site 1077 are not precise enough to determine the smectite crystallinity. The clay-mineral association in the Congo Basin area is controlled mainly by the varying contribution of these poorly crystallized smectites (van der Gaast and Jansen, 1984). Similar to Sites 1075 and 1076, low smectite values suggest significant low-crystalline contributions to the overall mineral association. Comparison of the $K/(K+Sm)$ ratios with the kaolinite and smectite intensities shows that the peaks in the ratio represent high kaolinite counts that are not diluted by large amounts of low-crystalline smectite (Fig. 3). Because kaolinite is a known product of chemical weathering of igneous rocks in the tropical rain forest (Singer, 1984), the high ratios suggest humid periods in the Congo drainage area, whereas the lower ratios represent more arid periods.

Spectrophotometry

Color data were measured every 2 cm for Hole 1077A. Hole 1077B was measured at 4-cm intervals. The reflectance data range between 25% and 45% throughout the column recovered from Site 1077. The total reflectance (Fig. 4) and red/blue (650/450 nm) ratio (Fig. 5) data were smoothed over nine points for Hole 1077A and over five points for Hole 1077B to remove smaller scale variability.

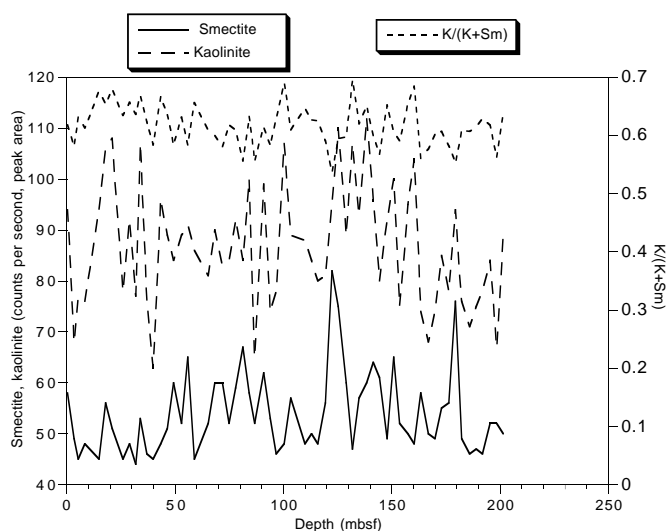


Figure 3. Stratigraphic variation in the ratio of smectite (Sm) to kaolinite (K), expressed as $K/(Sm+K)$.

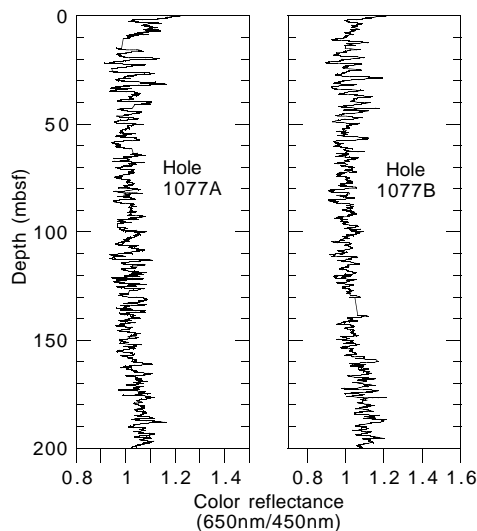


Figure 4. Stratigraphic variation in the ratio of the red (650 nm) to blue (450 nm) wavelengths at Holes 1077A and 1077B, displaying a pronounced periodicity that may correspond to the 23-k.y. precession cycle. A five-point smoothing procedure was applied to the data set.

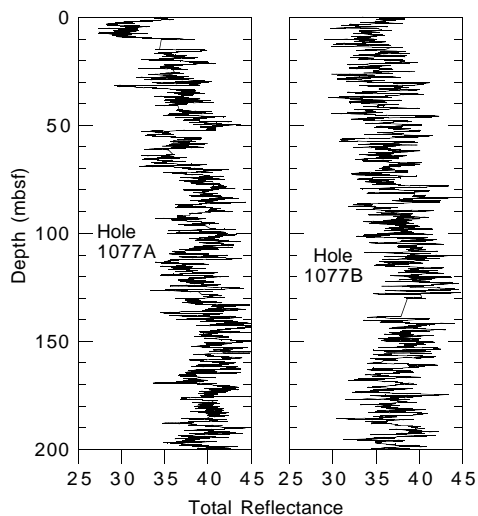


Figure 5. Stratigraphic variation in the total reflectance of visible light (400–700 nm) at Holes 1077A and 1077B, displaying a periodicity that may correspond to the 41-k.y. (obliquity) and 100-k.y. (eccentricity) cycles. A nine-point smoothing procedure was applied to the data set.

Total reflectance covaries with magnetic susceptibility (see Fig. 6), GRAPE density (see “Physical Properties” section, this chapter), and the downhole logging of the gamma-ray intensity at Hole 1077A (see “Downhole Logging” section, this chapter). Increased magnetic susceptibility, GRAPE density, and gamma-ray intensity suggest a relative increase in the clay component. If clay content were the only controlling parameter for total reflectance, then an increase in the clay component would decrease the total reflectance. The opposite is observed; therefore, total reflectance must be caused by variations in the other sediment components such as (1) the organic carbon content, (2) the biogenic component, which at Site 1077 is dominated by diatoms, and/or (3) the authigenic minerals. Organic matter is known to have a typically low reflectance in the visible domain and a high reflectance for the red to near-infrared domain (Mix et al., 1992). No

clear relation, however, is observed between the red/blue ratio and organic carbon contents (Fig. 7C). There is less information available about the influence of biogenic silica. The carbonate might control the red/blue ratio for the sediments with calcium carbonate concentrations >4 wt% (Fig. 7B). These higher weight percentages are relatively rare in sediments from this area (Jansen et al., 1984). For samples with lower carbonate concentrations, the comparison between sulfur and total reflectance shows a slightly positive relationship that suggests the influence of authigenic minerals on total reflectance (Fig. 7B). No correlation with pyrite, as measured with XRD, is observed. Despite the weak correlation between sulfur and total reflectance, we suggest that the lower total reflectance values measured during periods of relative reduced abundance of clay may reflect a relative increase of authigenic minerals present in the sediments, which is the result of there originally having been high levels of organic matter in the sediment. Shore-based work is required to discover the mechanism controlling the trends in the color data.

According to the biozones (see “Biostratigraphy and Sedimentation Rates” section, this chapter), intervals with high values of total reflectance and magnetic susceptibility generally correspond to interglacial stages (Fig. 6). Conversely, low values of total reflectance and magnetic susceptibility correspond to glacial stages. Using the ages provided by the “Biostratigraphy and Sedimentation Rates” and “Paleomagnetism” sections (this chapter), the periodicity in the red/blue ratio seems to be dominated by the 23-k.y. period (see Figs. 1, 6), whereas total reflectance and magnetic susceptibility records show longer periodicities. We suspect, therefore, that color is dominated by mechanisms tied to wind-driven productivity changes, while total reflectance and magnetic susceptibility are linked to fluctuations in sea level.

BIOSTRATIGRAPHY AND SEDIMENTATION RATES

Sediment recovered from Site 1077 represented a continuous hemipelagic section spanning the entire Pleistocene. According to paleomagnetic and nannofossil evidence, drilling at Site 1077 did not penetrate the Pliocene/Pleistocene boundary; the oldest sediment recovered was between 1.67 and 1.77 Ma. Micropaleontological studies were carried out on core-catcher samples from Hole 1077A. Additional samples from within the cores were examined for calcareous nannofossil- and silicoflagellate-based biostratigraphy.

Abundance and preservation varies between the different microfossil groups. Benthic foraminifers are abundant and well preserved down to Core 175-1077A-13H, calcareous nannofossils down to Core 15H, and planktonic foraminifers down to Core 17H. Siliceous microfossils are abundant and well preserved throughout Hole 1077A.

Both planktonic and benthic foraminiferal assemblages display a major change at an approximate depth of 52 mbsf.

Calcareous Nannofossils

The nannofossil-derived stratigraphy is based on a high-resolution study of Hole 1077A. The overall abundance ranges from abundant to common from Core 175-1077A-1H through 14H and generally decreases from Core 15H to the base of Hole 1077A. Preservation follows the same pattern, with well-preserved specimens in the upper half of the section, to moderately and poorly preserved assemblages within the bottom half of the hole. Only a few samples examined are barren. All identified datums could, therefore, be constrained within a narrow depth range of ~4 m (Table 2).

The nannofossil biostratigraphy suggests that drilling at Site 1077 recovered a continuous stratigraphic record spanning the entire Pleistocene (Zones NN21b–NN19). Paleomagnetic data (see “Paleomag-

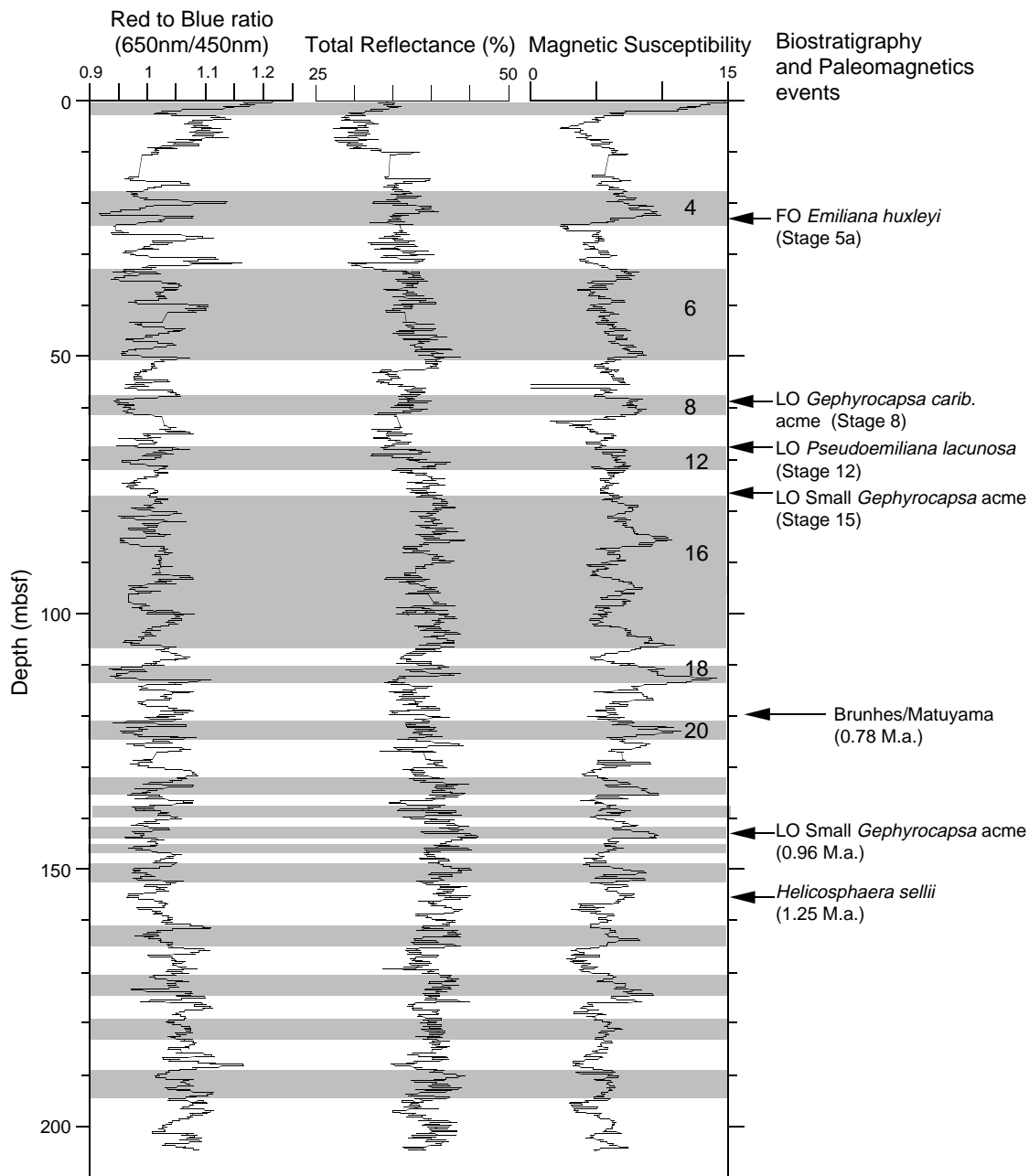


Figure 6. Comparison of the total reflectance and red/blue ratio with magnetic susceptibility vs. depth for Hole 1077A. Shaded areas show interglacial intervals and associated oxygen-isotopic stages as suggested from biostratigraphic and paleomagnetic events.

netism" section, this chapter) indicate that Hole 1077A did not penetrate the Olduvai polarity Chron, the termination of which identifies the Pliocene/Pleistocene boundary (1.77 Ma). The onset of this chron (1.95 Ma) is synchronous with the Zone NN19/NN18 boundary, as shown by Berggren et al. (1995). *Discoaster brouweri*, whose last occurrence (LO) is used as the datum event for this boundary, is not recognized in samples from the bottom of Hole 1077A nor in additional core-catcher samples from the bottom part of Hole 1077B, thereby confirming the paleomagnetic-derived stratigraphy.

Sedimentation rates estimated from nannofossil datum events suggest that sediments representative of Zone NN21 (last 260 k.y.) and of the upper half of Zone NN19 (960–600 ka) accumulated at an average rate of 20 cm/k.y. This pattern is interrupted during Zone

NN20 (460–260 ka) and the lower half of Zone NN19, where sedimentation rates are significantly lower (<5 cm/k.y.).

Zone NN21b

This dominance interval of *Emiliana huxleyi* is restricted to the top three cores of Hole 1077A (bottom of Zone NN21b, between Samples 175-1077A-3H-6, 70 cm, and 3H-CC).

Zone NN21a

This interval spans the lower half of isotope Stage 5 to the upper half of isotope Stage 8 (i.e., from 0.09 to 0.26 Ma). The Zone NN21a/

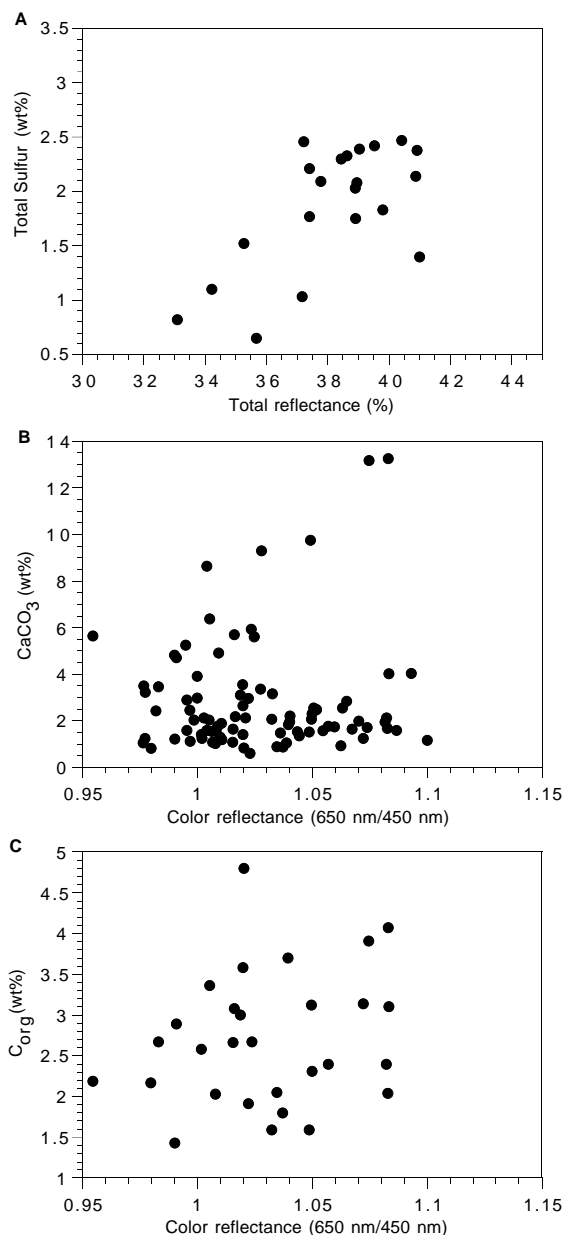


Figure 7. Relationship between (A) the total reflectance and total sulfur at Hole 1077A (values for total reflectance correspond to low calcium carbonate weight percent [<4 wt%] characteristic of the sediment from Site 1077). Relationship between red/blue wavelength spectral ratio and the concentrations of (B) calcium carbonate and (C) organic carbon at Hole 1077A.

NN20 boundary was reached in Hole 1077A at 58.32 mbsf (between Samples 175-1077A-7H-3, 130 cm, and 7H-5, 130 cm).

Zone NN20

As already noted at Sites 1075 and 1076, sediments representative of this interval accumulated at a very low rate (~ 3 cm/k.y.) compared with younger sediments. The Zone NN20/NN19 boundary, which is defined by the LO of *Pseudoemiliana lacunosa* (0.46 Ma; i.e., within isotope Stage 12) was reached between Samples 175-1077A-7H-CC and 8H-3, 130 cm.

Zone NN19

Five datum events were identified within this interval at Hole 1077A. The nannofossil chronology compares favorably with the position of the paleomagnetic chron boundaries (Fig. 8) for this interval. The depth-lag (~ 10 m) between the LO Small *Gephyrocapsa* acme event (0.96 Ma; Gartner, 1977) and the termination of the Jaramillo Chron (0.99 Ma) may be partly explained by the low sampling resolution in the vicinity of the nannofossil datum event.

Planktonic Foraminifers

The fauna at Site 1077 is not as strongly affected by dissolution as that at the other Congo Basin Sites 1075 and 1076. There are only two barren samples (Samples 175-1077A-19H-CC and 22H-CC) and one with poor preservation (Sample 175-1077A-18H-CC) at Hole 1077A.

The uppermost sample (175-1077A-1H-CC) is dominated by *Orbulina universa* with high abundances of *Globigerinoides ruber* (pink) and *Globorotalia inflata* (10%–30% of the population; Table 3). Other species present in significant abundance (5% or more of the total) include *G. ruber* (white), *Globigerinoides sacculifer*, *Globorotalia crassaformis*, *Globigerinella siphonifera*, and *Neogloboquadrina pachyderma* (dextral).

Downcore faunal variations at Hole 1077A suggest a change in the hydrographic regime below Core 175-1077A-7H-CC. Abundant *Globorotalia inflata* has been correlated to the Angola-Benguela Front (ABF; Jansen et al., 1996); possibly, its abundance may be used to trace the position of the ABF downcore. The species is abundant in the upper 52 mbsf (Samples 175-1077A-1H-CC, 3H-CC, 5H-CC, and 6H-CC) and at 127.5 mbsf (Sample 175-1077A-14H-CC). The decrease in abundance at ~ 50 mbsf suggests that the position of the ABF changed; it may represent a stabilization of the ABF in its present position. A change in benthic fauna occurs at the same depth.

O. universa and *N. pachyderma* (dextral) are abundant in nearly all samples downcore. *O. universa* is found in very high abundances in the Benguela Current region (Bé and Tolderlund, 1971). *N. pachyderma* is an indicator of upwelling in the tropics, along with abundant *G. bulloides* and *N. dutertrei* (Mix and Morey, 1996). High abundances of *G. ruber* (pink and white) in the tropics are associated with warm tropical conditions (Mix and Morey, 1996). *G. bulloides* is abundant downcore in Samples 175-1077A-5H-CC, 12H-CC, 13H-CC, 15H-CC, and 21H-CC and indicates high productivity associated with upwelling. *G. crassaformis* is a major component of the assemblage at the shallower water site (1076) but is not significant here, with the exception of a single excursion in Sample 175-1077A-3H-CC.

Benthic Foraminifers

The benthic foraminifers are well preserved and abundant in the upper 13 core catchers of Hole 1077A (Samples 175-1077A-1H-CC through 13H-CC), except for Sample 9H-CC, which contains very few specimens. Farther downcore, the abundance is significantly lower, and the lowermost four core catchers (Samples 175-1077A-19H-CC through 22H-CC) contain only a few benthic foraminifers or are completely barren.

As at Sites 1075 and 1076, the diversity of benthic foraminifers deteriorates downcore as a result of lower absolute abundance. This results in major difficulties when interpreting the variation in relative abundance of the various species. In the upper 50 mbsf of Hole 1077A, *Bulimina aculeata*, *Cassidulina laevigata*, *Melonis barleanum*, *Oridorsalis umbonatus*, and *Uvigerina hispidocostata* are the dominant species (Table 4; Fig. 9). Below 50 mbsf, the species *B. aculeata* disappears and is replaced by *Bulimina exilis* and *Melonis pompilioides* as dominant species. The contribution of *Cassidulina*

Table 2. Microfossil datums at Hole 1077A.

Fossil group	Event	Age (Ma)	Zone (base)		Core, section, interval (cm)		Depth (mbsf)		
			A	B	Top	Bottom	Top	Bottom	Mean
N	FO <i>Emiliana huxleyi</i> acme	0.09	NN21b		175-1077A-3H-6, 70	175-1077A-3H-CC	22.70	24.09	23.40
N	FO <i>Emiliana huxleyi</i>	0.26	NN21a	CN15	7H-3, 130	7H-5, 130	56.80	59.84	58.32
N	LO <i>Gephyrocapsa caribbeana</i> acme	0.26	NN21a	CN15	7H-3, 130	7H-5, 130	56.80	59.84	58.32
N	LO <i>Pseudoemiliana lacunosa</i>	0.46	NN20	CN14b	7H-CC	8H-3, 130	62.55	66.30	64.43
R	LO <i>Axoprunum angelinum</i>	0.46			7H-CC	8H-CC	62.55	72.24	67.39
N	LO Small <i>Gephyrocapsa</i> acme (Weaver, 1993)	0.60*			7H-CC	9H-3, 130	72.24	75.80	74.02
S	LO <i>Bachmannocena quadrangula</i>	0.80			12H-CC	13H-CC	110.14	119.47	114.81
N	LO <i>Reticulofenestra asanot</i>	0.83			13H-6, 10	13H-CC	117.10	119.47	118.29
N	LO Small <i>Gephyrocapsa</i> acme (Gartner, 1977)	0.96		CN14a	16H-3, 10	16H-CC	141.10	148.28	144.69
R	LO <i>Lamprocyrtis neoheteroporos</i>	1.07			18H-CC	19H-CC	166.73	176.39	171.56
N	LO <i>Helicosphaera sellii</i>	1.25			17H-6, 10	17H-CC	154.80	157.55	156.18
N	LO <i>Calcidiscus macintyre</i>	1.67			18H-6, 120	18H-CC	165.70	166.73	166.22

Notes: Fossil group: N = calcareous nannofossils; S = silicoflagellates; and R = radiolarians. FO = first occurrence and LO = last occurrence. * = middle isotope Stage 15 (Weaver, 1993); age interpolated from Imbrie et al. (1984). Zonal codes refer to the standard calcareous nannofossil zonations of (A) Martini (1971) and (B) Okada and Bukry (1980).

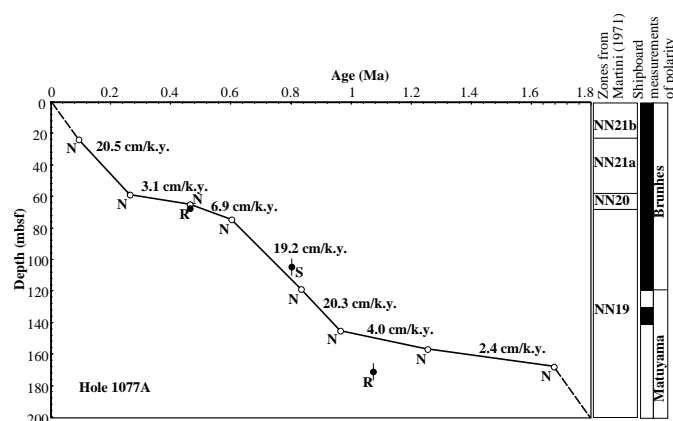


Figure 8. Age-depth plot and sedimentation rates at Hole 1077A estimated from calcareous microfossils (open circles; N = calcareous nannofossils) and siliceous microfossils (closed circles; S = silicoflagellates and R = radiolarians).

laevigata, *Melonis barleeianum*, *Oridorsalis umbonatus*, and *Uvigerina hispidocostata* is less pronounced. Other species are present in low relative abundances and/or are present only in a few samples.

Radiolarians

Radiolarians are present in all of the core-catcher samples from Hole 1077A (Table 5). Radiolarian abundance is common to abundant, and preservation is good. No apparent reworking has been identified.

The radiolarian fauna indicates a Quaternary age for Hole 1077A. The absence of *Axoprunum angelinum* suggests that the uppermost cores (175-1077A-1H-CC through 7H-CC) are within either the Pleistocene *Collosphaera tuberosa* Zone or the Pleistocene to Holocene *Buccinosphaera invaginata* Zone of Moore (1995). A finer zonal resolution could not be achieved because of the absence of *B. invaginata*.

Although the diagnostic species *Anthocyrtidium angulare* is absent throughout the core, Samples 175-1077A-8H-CC through 18H-CC are assigned to the Pleistocene *A. angelinum* Zone or *Amphirhopalum ypsilon* Zone of Moore (1995) based on the presence of *A. angelinum* and the absence of *Lamprocyrtis neoheteroporos*. The diagnostic species *C. tuberosa*, used to recognize the *A. angelinum* and *A. ypsilon* Zones, is absent from Samples 8H-CC through 18H-CC. A LO of *L. neoheteroporos* is found in Sample 175-1077A-19H-CC,

Table 3. Dominant and abundant planktonic foraminiferal species at Hole 1077A.

Core, section, interval	Depth (mbsf)	Species									
		<i>Globigerinoides ruber</i> (pink)	<i>Globigerinoides ruber</i>	<i>Orbulina universa</i>	<i>Globigerina bulloides</i>	<i>Globigerinella siphonifera</i>	<i>Globobulimina inflata</i>	<i>Globobulimina menardii</i>	<i>Neoglobobulimina duerrei</i>	<i>Neoglobobulimina pachyderma</i> (dextral)	<i>Globobulimina crassaformis</i>
175-1077A-1H-CC	4.93	A	D				A				
2H-CC	10.78	A	A	A							
3H-CC	24.09	A	A				A	A	A	A	
4H-CC	33.85	A						A	A		
5H-CC	43.39		A	A	A		A				
6H-CC	52.93		A	A			A		A		
7H-CC	62.55		A	D					A		
8H-CC	72.22		A	A					D		
9H-CC	80.89			A		A			A		
10H-CC	91.06		A	A					A		
11H-CC	100.46		A	A					A		A
12H-CC	110.14		A	A	A	A			A	A	
13H-CC	119.47		A	A	D	A			A	A	
14H-CC	127.47						A	A		D	
15H-CC	138.67			D	A	A			A	A	
16H-CC	148.28			A	A			A	A	A	
17H-CC	157.55				D		A				
18H-CC	166.73										
19H-CC	176.39										
20H-CC	185.93			A			A		A	D	
21H-CC	195.49			A	A	A			A	A	
22H-CC	205.01										

Note: D = dominant (>30% of the population) and A = abundant (10%–30%).

indicating an age older than 1.07 Ma for Samples 19H-CC through 22H-CC. The single occurrence of *A. angulare* in Sample 16H-CC can place the upper boundary of the *A. angulare* Zone somewhere between Samples 15H-CC and 16H-CC. The LO of *L. neoheteroporos* is more reliable and useful for correlating Holes 1075A, 1076A, and 1077A, and the upper boundary of the *A. angulare* Zone is tentatively placed between Samples 18H-CC and 19H-CC.

Diatoms

Diatoms are the dominant microfossil group at Hole 1077A. Species counts and identification were carried out on smear-slides. In ad-

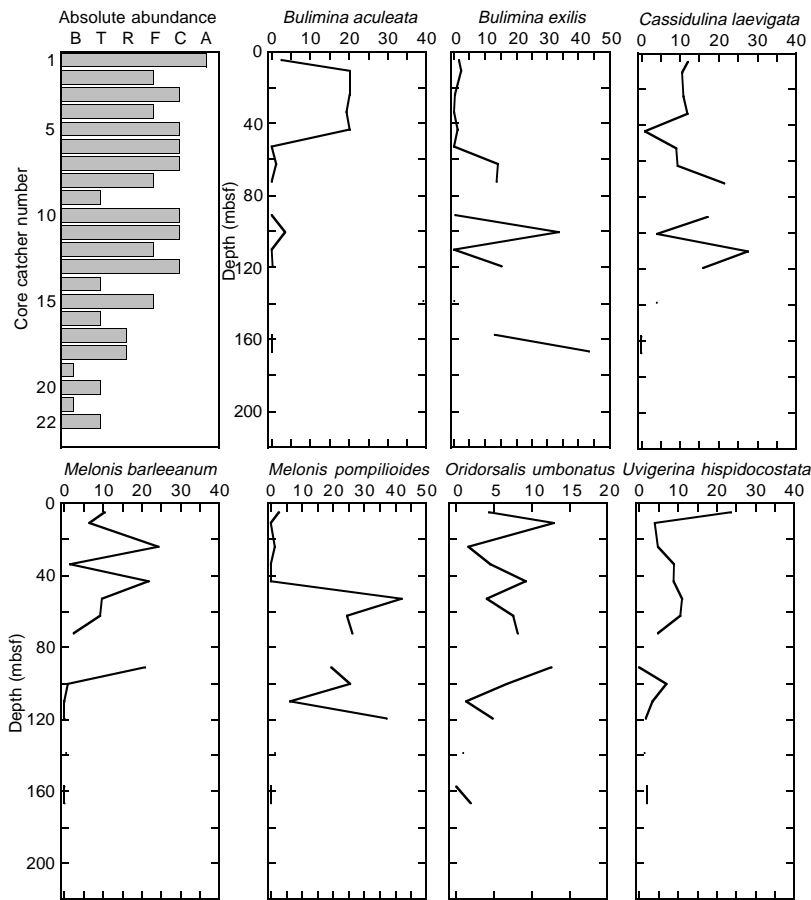


Figure 9. Relative abundances in percent for selected benthic foraminiferal species. Absolute abundance (per ~20 cm³ of sediment) of benthic foraminifers are given as A = abundant (>500 specimens); C = common (250–500 specimens); F = few (100–249 specimens); R = rare (50–99 specimens); T = trace (1–49 specimens); and B = barren (no specimens). Note that some samples are barren or contain very few specimens (Samples 175-1077A-9H-CC, 14H-CC, 16H-CC, and 19H-CC through 22H-CC) and that no reliable percentage estimates could be obtained.

Table 5. Stratigraphic distribution of radiolarians at Hole 1077A.

Age	Zone	Core, section, interval	Depth (mbsf)	Abundance	Preservation	<i>Cycladophora comutoides</i>	<i>Cycladophora davisi</i>	<i>Didymocypris tetrathalamus tetrathalamus</i>	<i>Eucyrtidium acuminatum</i>	<i>Eucyrtidium anomalum</i>	<i>Eucyrtidium teuscheri</i>	<i>Lamprocyclus hainai</i>	<i>Lamprocyrtis nigrinae</i>	<i>Phormostichoartus corbula</i>	<i>Pterocanium praetextum eucolpum</i>	<i>Pterocanium trilobum</i>	<i>Satumalis circularis</i>	<i>Spongaster tetras tetras</i>	<i>Theocyrtidium trachelium trachelium</i>	<i>Acanthodesmia vinctulata</i>	<i>Eucyrtidium calvertense</i>	<i>Pterocanium praetextum praetextum</i>	<i>Amphirhopalum ypsilon</i>	<i>Collosphaera tuberosa</i>	<i>Axoprunum angelinum</i>	<i>Anthocyrtidium angulare</i>	<i>Lamprocyrtis heteropora</i>	<i>Lamprocyrtis neoheteropora</i>	
Quaternary	<i>B. invaginata</i> – <i>C. tuberosa</i>	175-1077A-1H-CC	4.93	A	G	P	P	P	P	P	P	P	+	+	+	P	P	P	P	P									
Quaternary	<i>B. invaginata</i> – <i>C. tuberosa</i>	2H-CC	10.78	A	G	P	P	P	+	P	P	P	P			P	P	P	P	P									
Quaternary	<i>B. invaginata</i> – <i>C. tuberosa</i>	3H-CC	24.09	A	G	P	P	P	P	+	+	P	P			P	P	P	P	P									
Quaternary	<i>B. invaginata</i> – <i>C. tuberosa</i>	4H-CC	33.85	A	G	P	P	P	P	P						P	P	P	P	P									
Quaternary	<i>B. invaginata</i> – <i>C. tuberosa</i>	5H-CC	43.39	A	G	+	P	P			P	P	P	+	P	P	P	P	P	P									
Quaternary	<i>B. invaginata</i> – <i>C. tuberosa</i>	6H-CC	52.93	C	G	P	P	+	P	+	P	P	P	+	P	P	P	P	P	P									
Quaternary	<i>B. invaginata</i> – <i>C. tuberosa</i>	7H-CC	62.55	A	G	P	P	P	P	P	+	P	P	P	P	P	P	P	P	P									
Pleistocene	<i>A. angelinum</i> – <i>A. ypsilon</i>	8H-CC	72.22	A	G	P	P	P	P	+	P	P	P		P	P	+	P	P	+	P								P
Pleistocene	<i>A. angelinum</i> – <i>A. ypsilon</i>	9H-CC	80.89	A	G	P	P	P	P		P	P	P		P	P	P	P	P	P									P
Pleistocene	<i>A. angelinum</i> – <i>A. ypsilon</i>	10H-CC	91.06	C	G	P	P	P	P		P	P	P		P	P	+	+	+	+									P
Pleistocene	<i>A. angelinum</i> – <i>A. ypsilon</i>	11H-CC	100.46	A	G	P	P	P	P		P	P	P		P	P	+	P	+	+									P
Pleistocene	<i>A. angelinum</i> – <i>A. ypsilon</i>	12H-CC	110.14	A	G	P	P	P	P		P	P	P		P	P	+	P	+	+									P
Pleistocene	<i>A. angelinum</i> – <i>A. ypsilon</i>	13H-CC	119.47	A	G	P	P	P	P		+	P		+	P	P	+	+	+	+									+
Pleistocene	<i>A. angelinum</i> – <i>A. ypsilon</i>	14H-CC	127.47	A	G	P	P	P	P		P	P			P	P													+
Pleistocene	<i>A. angelinum</i> – <i>A. ypsilon</i>	15H-CC	138.67	A	G	P	P	P	P		P	P		+	P	P	+	P		P									+
Pleistocene	<i>A. angelinum</i> – <i>A. ypsilon</i>	16H-CC	148.28	A	G	P	P	P	P	P	P	P			P	P		P	P										+
Pleistocene	<i>A. angelinum</i> – <i>A. ypsilon</i>	17H-CC	157.55	A	G	+	P	P	+	+	+	P	P		P	P		P	P									+	
Pleistocene	<i>A. angelinum</i> – <i>A. ypsilon</i>	18H-CC	166.73	A	G	P	P	P	P	P	P	P			P	P		P	P										+
Pleistocene	<i>A. angulare</i>	19H-CC	176.39	A	G	P	P	P	P		P	P			P	P	+	+		P									P
Pleistocene	<i>A. angulare</i>	20H-CC	185.93	C	G	P	P	P	P		P	P			P	P		P	+										+
Pleistocene	<i>A. angulare</i>	21H-CC	195.49	C	G	P	P	P	P	+	P	P			P	P		+											+
Pleistocene	<i>A. angulare</i>	22H-CC	205.01	A	G	P	P	P	P		P	P			P	P		+	P										+

Notes: Occurrence is indicated by P = present and + = one specimen per slide. Abundance: A = abundant and C = common. Preservation: G = good. *B. invaginata* = *Buccinosphaera invaginata*; *C. tuberosa* = *Collosphaera tuberosa*; *A. angelinum* = *Axoprunum angelinum*; *A. ypsilon* = *Amphirhopalum ypsilon*; *A. angulare* = *Anthocyrtidium angulare*.

dition, opaline phytoliths and silicoflagellates were also counted without distinction of species or morphotypes. In general, diatoms are abundant and well preserved throughout Hole 1077A, except for in Sample 175-1077A-14H-CC (Table 6). Examination of the core-catcher samples indicates a Pleistocene age for this hole. Samples 175-1077A-1H-CC through 12H-CC are assigned to the *Pseudoeunotia doliolus* Zone, and Samples 175-1077A-15H-CC through 21H-CC to the *Nitzschia rheinholdii* Zone. A diatom biostratigraphic marker species is lacking from Samples 175-1077A-13H-CC, 14H-CC, and 22H-CC. The silicoflagellate *Mesocena quadrangula* is, however, present in Samples 13H-CC (LO, 0.8 Ma) through 16H-CC (first common occurrence at 1.0 Ma; Locker, 1996) and may be used as a biostratigraphic marker instead. This is in agreement with paleomagnetic data for Hole 1077A (see "Paleomagnetism" section, this chapter).

The diatom flora is dominated by upwelling-indicator species (>50% of total diatom assemblage *Thalassionema nitzschioides* var. *nitzschioides* and *Chaetoceros* resting spores and setae; see Table 6; Fig. 10), accompanied by freshwater taxa (e.g., *Aulacoseira granulata*, *A. islandica*, and *Cyclotella* spp.) and neritic species (e.g., *Actinopterychus senarius*). Two distinct pulses of the coastal species *Skeletonema costatum* are observed in Samples 175-1077A-4H-CC (~32%) and 8H-CC (~21%), respectively; a single peak of *Thalassiosira* spp. (mainly *T. eccentrica* and *T. oestrupii*) is seen in Sample 4H-CC. In general, diatom assemblages characterize Hole 1077A as a coastal upwelling site with variable freshwater input (Fig. 10).

As at Holes 1075A and 1076A, the presence of freshwater diatoms at Hole 1077A is attributed to supply by the Congo River, and high abundances may be interpreted as signals for humid intervals on the African continent (e.g., Jansen et al., 1989). The average contribution of the freshwater assemblage is somewhat higher here (7.2%) than at Sites 1075 and 1076. The abundance pattern is similar at Site

1076, with two large peaks (~30%) in the upper 50 mbsf at Hole 1077A and a third peak at ~100 mbsf. Opaline phytoliths are rare (Table 6).

PALEOMAGNETISM

The investigation of magnetic properties at Site 1077 included the measurement of bulk susceptibility of whole-core sections and the natural remanent magnetization (NRM) of archive-half sections. The Tensor tool was used to orient Holes 1077A and 1077B, starting with the fourth core (Table 7).

Natural Remanent Magnetization and Magnetic Susceptibility

Measurements of NRM were made on all archive-half core sections from Holes 1077A, 1077B, and 1077C. Sections from Hole 1077A were demagnetized by AF at 10 and 20 mT, and sections from Holes 1077B and 1077C were demagnetized by AF at 20 mT only.

Magnetic susceptibility measurements were made on whole cores from all three holes as part of the MST analysis (see "Physical Properties" section, this chapter). Magnetic susceptibility is on the order of 10⁻⁵ (SI volume units; Fig. 11).

The intensity of NRM after 20-mT demagnetization from Holes 1077A and 1077B is similar in magnitude, ranging from ~10⁻⁵ to ~10⁻³ A/m (Fig. 12, left panel). Within the upper 80 mbsf, the intensity is on the order of 10⁻³ to 10⁻⁴ A/m. Between 80 and 140 mbsf, the intensity fluctuates between ~10⁻⁴ A/m and ~10⁻⁵ A/m, after which it remains relatively constant (on the order of 10⁻⁵ A/m) with depth. The magnetic susceptibility does not show these trends but remains fairly constant at about 4 × 10⁻⁵ throughout Holes 1077A and 1077B.

A primary magnetic component was preserved in the majority of the sediments from Holes 1077A and 1077B, which allowed us to determine the magnetic polarity. Directions of the NRM below ~120 mbsf, however, show relatively large scatter, suggesting the presence

Table 6. Overall diatom abundance and relative contribution of the dominant species or assemblages at Hole 1077A.

Core, section, interval	Depth (mbsf)	Overall abundance	Overall preservation	<i>Thalassionema nitzschioides</i> (%)	<i>Chaetoceros</i> resting spores (%)	<i>Skeletonema costatum</i>	<i>Thalassiosira</i> spp.	Freshwater assemblage (%)	Phytoliths	Silicoflagellates
175-1077A-1H-CC	4.93	A	M	32.5	34.0		T	21.8		T
2H-CC	10.78	A	G-M	17.8	38.4	T	R	22.7		T
3H-CC	24.09	A	G-M	50.7	39.6	R	R	3.35	T	T
4H-CC	33.85	C	M	35.5	13.3	31.8	T	8.6		T
5H-CC	43.39	A	M	40.4	25.0		T	27.1		T
6H-CC	52.93	A	M	47.6	36.8	T	T	4.7		T
7H-CC	62.55	C-F	M-P	61.7	25.7		R	3.3	T	T
8H-CC	72.22	C	M	20.9	38.6	21.4	R	4.8		T
9H-CC	80.89	C-F	M-P	37.0	41.5	T	R	1.5		T
10H-CC	91.06	C	M-P	34.0	42.7	T	T	10.9		T
11H-CC	100.46	A-C	M-P	31.7	42.2		T	13.4	T	T
12H-CC	110.14	C	M	31.4	44.1	T	R	6.9	T	T
13H-CC	119.47	A	M	65.8	26.6		T	4.4		T
14H-CC	127.47	F	M-P	60.6	17.4	T	R	3.7		T
15H-CC	138.67	A-C	M	55.1	29.9		T	0		T
16H-CC	148.28	A	M	61.9	31.5		T	2.7		T
17H-CC	157.55	A-C	G-M	64.7	28.6	T	R	2.3		T
18H-CC	166.73	A	M	34.1	52.5	T	F	3.7		R
19H-CC	176.39	C	M	18.3	54.2	T	17.5	4.1		T
20H-CC	185.93	A	M	51.0	30.3		R	5.4		T
21H-CC	195.49	A	M	28.8	34.9		T	0.7		T
22H-CC	205.01	A	M-P	31.8	40.5	T	R	1.7		T

Notes: Includes diatom upwelling and freshwater assemblages, opaline phytoliths, and silicoflagellates (in percentages). Abundance: A = abundant; C = common; F = few; T = trace; and R = rare. Preservation: M = moderate; G = good; and P = poor.

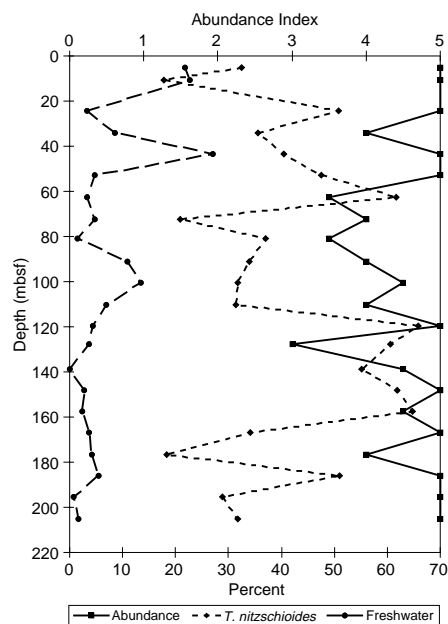


Figure 10. Diatom abundance (z-axis), and percent *T. nitzschioides* and freshwater diatoms (x-axis) at Hole 1077A. Abundance index: 5 = abundant, 4 = common, 3 = few, 2 = rare, 1 = trace, and 0 = barren. *T. nitzschioides* is an upwelling indicator in the Congo Fan area.

Table 7. Tensor tool-orientation data for cores from Holes 1077A and 1077B.

Core, section	MTF (°)	Inclination angle
175-1077A-		
4H	308	0.66
5H	290	0.19
6H	232	0.23
7H	273	0.70
8H	171	0.18
9H	274	0.44
10H	59	0.38
11H	260	0.44
12H	22	0.93
13H	350	1.75
14H	26	0.38
15H	14	0.37
16H	345	0.59
17H	260	0.36
18H	295	0.29
19H	239	0.28
20H	269	0.29
21H	74	0.44
22H	78	0.41
175-1077B-		
4H	27	1.47
5H	186	0.98
6H	252	1.19
7H	297	1.27
8H	125	1.12
9H	294	1.14
10H	175	1.16
11H	289	1.10
12H	195	1.00
13H	30	0.78
14H	230	1.25
15H	273	0.87
16H	357	0.81
17H	185	0.79
18H	144	0.77
19H	55	0.64
20H	170	0.67
21H	30	0.66
22H	141	0.44

Notes: The orientation parameter (MTF) is the angle in degrees between magnetic north and the double line marked on the center of the working half of the core. The local declination anomaly is 6°W.

of secondary magnetization. Part of a magnetic overprint acquired during coring still remains after 20-mT demagnetization (see below). Viscous remanent magnetization and/or chemical remanent magnetization caused by diagenetic growth or dissolution of magnetic minerals may also contribute to the secondary magnetizations.

Magnetostratigraphy

We identified the polarity of the NRM from the declinations and inclinations. Data from the Tensor orientation tool were available for most of Holes 1077A and 1077B, which facilitated interpretation of reversals in terms of the geomagnetic time scale. Changes of inclination with polarity transitions were difficult to interpret because of the relatively low latitude of this site (an inclination of -23° is expected from the geocentric axial dipole model) and the magnetic overprint (Fig. 12, right panel).

The Brunhes/Matuyama polarity transition (0.78 Ma; Berggren et al., 1995) occurs between 115 and 120 mbsf at Hole 1077A and between 112 and 118 mbsf at Hole 1077B (Fig. 12, middle and right panels). The thickness of sediments, which records a polarity transition, should be ~ 1.4 m at these holes, assuming that the sedimentation rate is ~ 140 m/m.y. and a polarity transition completes within 10 k.y. The large scatter of the remanent directions and the presence of unremoved secondary components, however, made it difficult to determine the exact position of the boundary. Below the Brunhes/Matuyama boundary, an interval of relatively well-grouped northward declinations occurs from ~ 128 to 137 mbsf at Hole 1077A and from ~ 128 to 138 mbsf

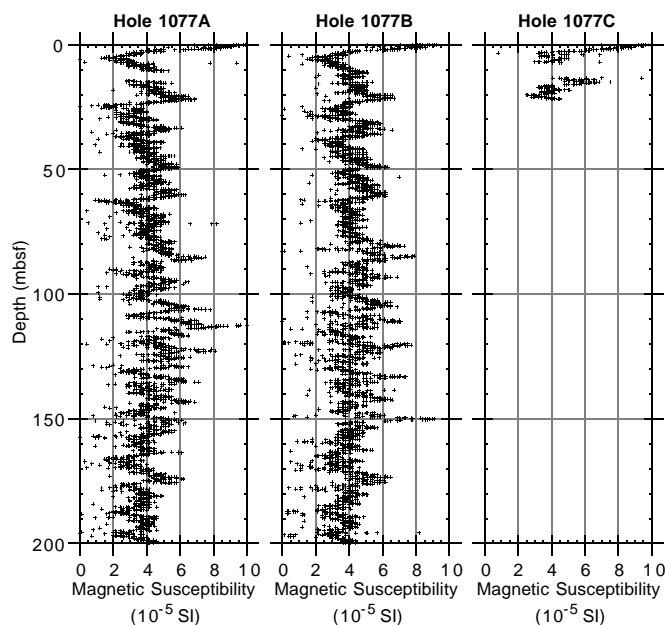


Figure 11. Magnetic susceptibilities from MST data (volume corrected) for Holes 1077A, 1077B, and 1077C.

at Hole 1077B. We tentatively interpret this as the Jaramillo Subchron (C1r.1n). This interpretation, however, does not agree with biostratigraphic data (see “Biostratigraphy and Sedimentation Rates” section, this chapter). There is a possibility that this interval contains coring magnetization, as discussed below. The scatter of directions is very large from ~ 137 to 155 mbsf at Hole 1077A and from 138 to 160 mbsf at Hole 1077B; thus, it is difficult to determine the polarity of magnetization.

Coring-Induced Magnetization

At this site, we encountered significant magnetic overprinting caused by the coring process. Figure 13 shows the NRM of Cores 175-1077B-17H through 22H (below 148 mbsf). Within each core, the inclination becomes positive and steeper upcore with a parallel increase in intensity. Deeper sections in each core show relatively well-grouped declinations, but shallower sections show larger scatter. These tendencies emerge at about 40 mbsf and become more pronounced with depth below seafloor.

Physical deformation of sediments caused by the core liner being dragged along the sediment during coring and/or sediment expansion after recovery can affect the direction and intensity of NRM (Shipboard Scientific Party, in press). Figure 14A illustrates that the effect of drag along the core-liner on the magnetic inclination is opposite in the archive and working halves: in this example, inclination steepens within the working half and shallows within the archive half as a result of coring disturbance along the rim. The angle between the split surface of the cores and the horizontal component of NRM varies with the orientation of cores. The orientation and intensity of the overprint are thus expected to depend on the orientation of cores in this model. In Holes 1077A and 1077B, however, the inclination always shifts to positive and downward in the upcore direction, independent of the core orientation. It is also difficult to explain the increase in intensity within each core by this model. It is thus concluded that this type of deformation is not responsible for the magnetic overprint.

During previous Ocean Drilling Program (ODP) legs, coring-induced magnetization (CIM) of radially inward and steep-down-

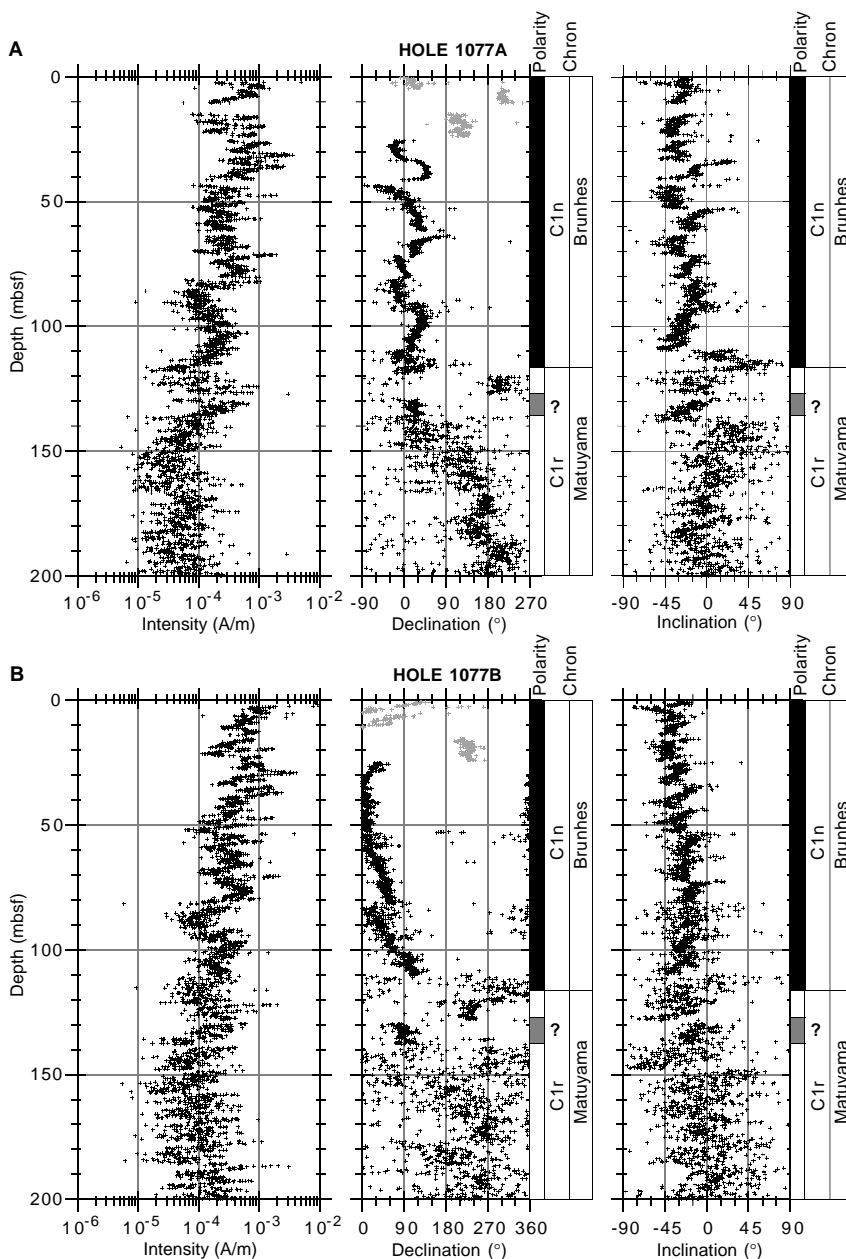


Figure 12. NRM intensity, declination, inclination, and magnetostratigraphic interpretation after 20-mT demagnetization for (A) Hole 1077A and (B) Hole 1077B. Black symbols = Tensor corrected; gray symbols = uncorrected. Polarity shading: black = normal, white = reversed, and gray = ambiguous.

ward directions has often been reported in sediments recovered with the APC (e.g., Curry, Shackleton, Richter, et al., 1995; Shipboard Scientific Party, 1996). During some legs, the CIM was much stronger in intensity than the primary NRM, and it could not be erased by AF demagnetization. This made it impossible to recover a meaningful geomagnetic signal from the sediments. Efforts to seek the cause and solution of the CIM have been made during recent legs (Fuller et al., 1997; Fuller and Garrett, in press). The magnetic overprint observed at this site could be explained by an upward increase in the CIM within each core. The acquisition of a steep downward overprint makes the inclination become positive and steeper, and it is independent of core orientation because of the radially inward component (Fig. 14B). Upcore increase of the acquisition of CIM suggests that a shearing stress during penetration under a magnetic field from the core barrel and the cutting shoe could produce the CIM, because sediments in the upper part of each core suffer from shear for a longer period of time than those from the lower part. This model can also ex-

plain the fact that the CIM is less evident in softer sediments at shallower depths below the seafloor.

To our knowledge, this is the first report of within-core variation of CIM, which could facilitate a better understanding of the origin of CIM. The upcore increase of intensity was already documented as an anomalous feature of the CIM during Leg 154 (Shipboard Scientific Party, 1995), but no trend in remanent directions was found because the very strong CIM dominated the NRM.

COMPOSITE SECTION

Two holes with a maximum penetration of 205.2 mbsf were cored with the APC at Site 1077. Hole 1077C was abandoned after retrieval of Core 175-1077-3H at 22 mbsf. Physical properties and color reflectance data were measured at 2-cm (Hole 1077A) and 4-cm (Hole 1077B and Hole 1077C) intervals. The correlation of features present

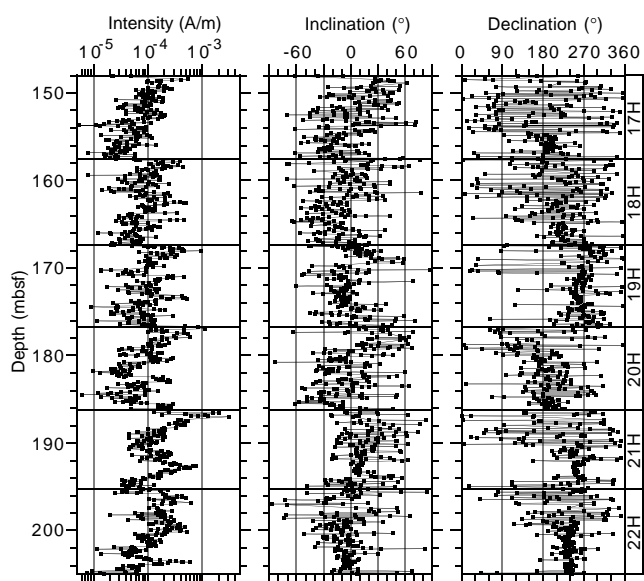


Figure 13. Intensity, inclination, and declination of Cores 175-1077B-17H through 22H. Cores were oriented by the Tensor tool.

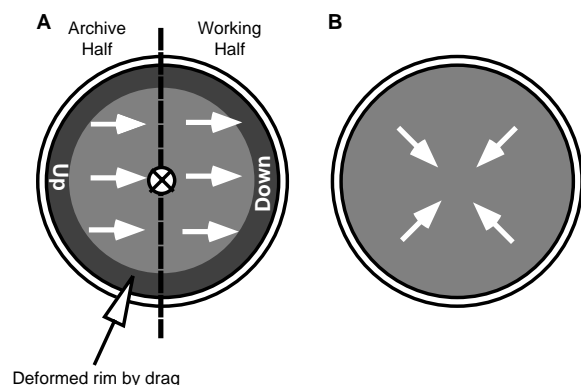


Figure 14 **A**. Effect of drag along core liner on inclination. Note that the effect is opposite between the right and left halves when core with declination (internal arrows) is split along the dashed line. **B**. Radial inward overprint associated with coring process (CIM).

in the physical and visual properties measurements of adjacent holes were used to demonstrate the completeness of the local stratigraphic sequence drilled and to establish a depth scale in terms of meters composite depth (mcd) for Site 1077. The continuity of the stratigraphic sequence was shown from 15 to 211 mcd. A gap of 1.2 m at 14 mcd is caused by poor recovery (60%) of Cores 175-1077A-2H and 175-1077C-2H (Fig. 15).

At Site 1077, magnetic susceptibility and red/blue ratio (650 nm/450 nm) calculated from color reflectance data were used to establish the mcd scale. The data sets were extensively processed before being used for correlation. Suspect measurements were eliminated by thresholding the data, followed by additional processing using a linear approximation filter algorithm. For 10 measurements, taken over an interval of 20 to 40 cm, a linear regression and the standard deviation of the data were calculated. Measurements with values outside twice the standard deviation were reassigned the linearly approximated value. Finally, the data were smoothed using a Gaussian filter with a length of 12 cm. All data shown in Figures 15 and 16 were processed as described above.

The double APC coverage at Site 1077 did not allow for the demonstration of a complete sedimentary record over the entire 205 mbsf drilled. In addition, the cores from Holes 1077A and 1077B did not overlap in an optimal fashion. The determination of the composite depth scale relies on the identification of features common to physical properties measurements in overlapping sections of adjacent cores. Where this was not possible, the driller's depth (in mbsf) was taken as composite depth (mcd). Cores 175-1077A-2H through 5H, and 175-1077B-2H, 6H, and 7H remained at their respective depth in mbsf (Figs. 14, 16, 17; also see Table 8). The strategy for the construction of the composite section was to combine depth information from Holes 1077A and 1077B in an optimal fashion. Where justified, the overlap between adjacent cores was increased to avoid the inclusion of data from the top and bottom ends of individual cores in the spliced record. In fact, an improvement of core overlap was possible only in a few depth intervals. The resulting growth of the mcd scale compared with the standard ODP mbsf scale is ~6%.

The spliced record presented in Figure 16 and Table 9 is continuous between 15 and 211 mcd for magnetic susceptibility and GRAPE wet bulk densities. The remaining data gaps within this depth interval are of decimeter to centimeter size and thus are considered negligible. The selection of cores to be included in the spliced record and the placement of tie points was carried out mainly using the composite section of magnetic susceptibility from Site 1077. The strategy for splicing was to construct a continuous spliced record with smooth transitions between individual cores for most of the cored depth interval.

INORGANIC GEOCHEMISTRY

Two sets of interstitial water samples were collected at Site 1077 (Table 10). First, 16 interstitial water samples were collected from Hole 1077A (1.5–203.9 mbsf) to provide coverage of diagenetic processes through the entire recovered sedimentary succession and to complete the three-site transect of the Congo Margin. The chemical distributions in interstitial waters at Site 1077 are very similar to those observed at Site 1075 and are only modestly distinct from those at Site 1076.

Second, a special high-resolution study, with interstitial water samples being gathered at a frequency of three per core, targeted the interval from ~100 to 130 mbsf with a total of nine additional samples. This depth range included a seismic reflector (see "Site Geophysics" section, "Site 1075" chapter, this volume) that potentially was caused by a thin (2–10 m in thickness) layer of methane hydrate. This study was intended to test whether hydrate was the cause of the seismic discontinuity.

Alkalinity, Sulfate, and Ammonium

As seen at both Sites 1075 and 1076, downcore profiles of alkalinity, sulfate, and ammonium (Fig. 18) reflect the degradation of organic matter. The general distribution of these interstitial water components records the shallow generation of alkalinity, in large part from consumption of sulfate, paired with a steady and consistent increase in ammonium. Although the deep increase in alkalinity found at Site 1076 was not observed at Site 1077, in all other aspects the behavior of these dissolved components records a chemical behavior intermediate in nature to those observed at Sites 1075 and 1076.

Calcium, Magnesium, and Strontium

The strong gradients in Ca^{2+} , Mg^{2+} , and Sr^{2+} that initially occur at shallower depths at Site 1077 (Fig. 19) record carbonate dissolution and reprecipitation reactions. The increase in dissolved Sr^{2+} above values of deep bottom-water reflects biogenic calcite dissolution, where-

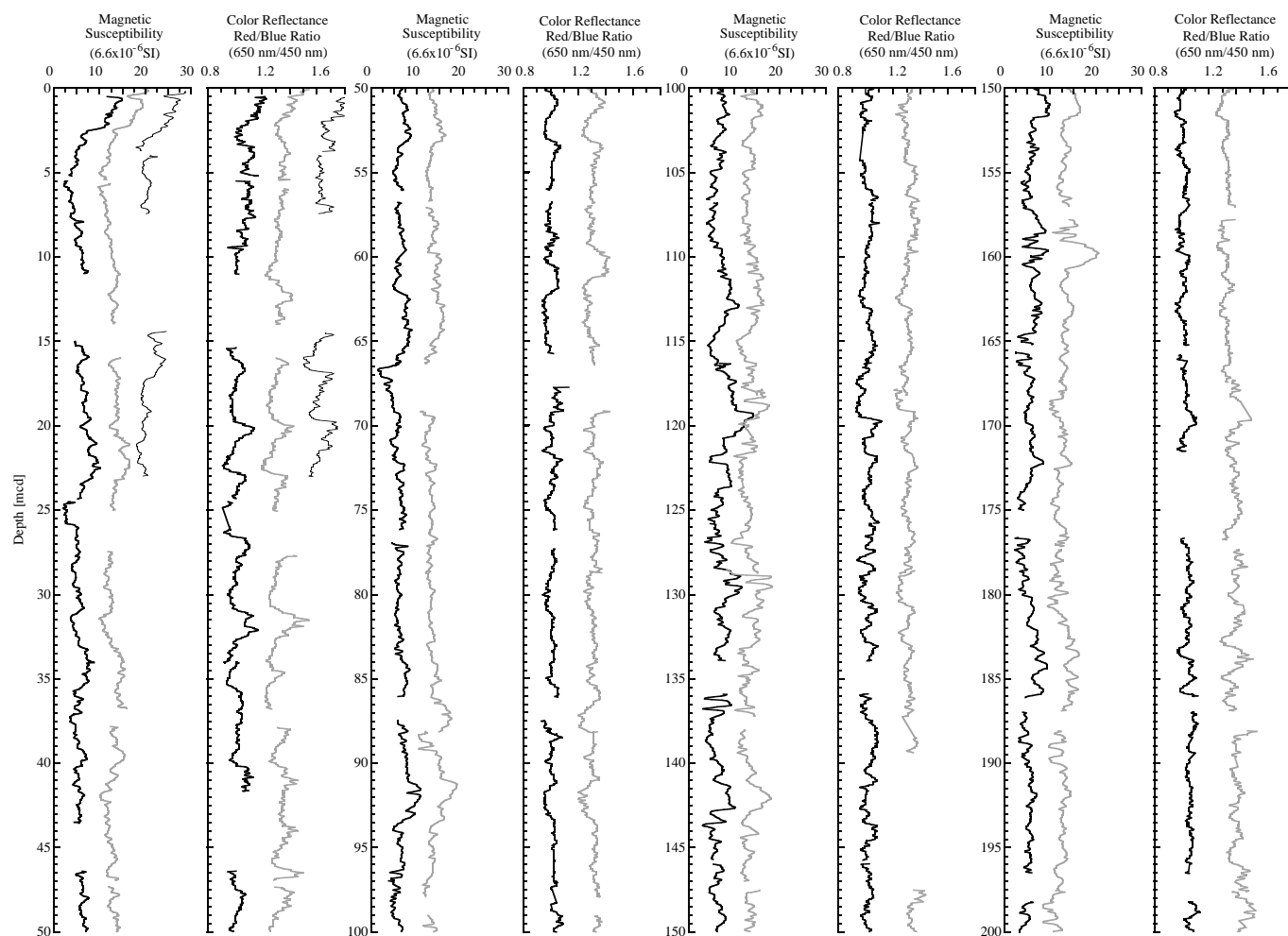


Figure 15. Composite section for Site 1077. Magnetic susceptibility and color reflectance (red/blue ratio [650 nm/450 nm]) are plotted for Holes 1077A (thick black line), 1077B (gray line), and 1077C (thin black line). The down-hole logs are shown in meters composite depth (mcd). Offsets have been applied for clarity.

as the decreases in dissolved Ca^{2+} and Mg^{2+} through the same interval most likely indicate precipitation of dolomite. Reflecting the commonality of processes operating at Sites 1077 and 1075, the chemical distributions in interstitial waters at these two sites are strongly similar. The only significant contrast between the two sites is a slight increase, at depth, in dissolved Sr^{2+} and Ca^{2+} at Site 1077, which collectively indicates a second phase of biogenic calcite dissolution.

Silica and Phosphate

Dissolved silica increases in concentration very rapidly through the uppermost 5 m of sediment (Fig. 20), recording the dissolution of biogenic opal. Concentrations continue to gradually increase at depth downcore. There appears to be no obvious relationship between this depth pattern and the distribution of diatoms in the sequence (see “Biostratigraphy and Sedimentation Rates” section, this chapter).

Dissolved phosphate increases very rapidly to a maximum value of $\sim 250 \mu\text{M}$ within the uppermost 20 mbsf. This rate of increase is much sharper than that at Site 1075 or Site 1076, both also located in the Congo Basin. This is somewhat surprising, given that the increase in alkalinity and the consumption of sulfate at Site 1077 are approximately the same as at the other sites. This contrast may reflect differences in the organic matter-to-clay ratio, in the amount of diagenetic apatite that is forming, or in some other analogous solid phase variation that would serve to create a different production-to-removal balance. One potentially important indicator is glauconite; Site 1077 has

appreciably greater quantities of this phase (see “Lithostratigraphy” section, this chapter), which is preferentially found in nutrient-rich upwelling regions. Although the TOC concentrations at Site 1077 are similar to those at Sites 1075 and 1076, the TOC value is a bulk measurement and therefore may not detect subtle variations in organic matter composition that are manifest in the inorganic solid phase mineralogy. An additional consideration is the fact that although the maximum in dissolved phosphate is notably greater at Site 1077, the concentrations at depth are approximately the same as at the other sites. Therefore, the removal of dissolved phosphate at Site 1077 is also greater. We postulate, therefore, that postcruise mineralogical studies will find greater concentrations of solid phase, phosphate-bearing minerals as well.

Sodium and Potassium

Concentrations of dissolved Na^+ and K^+ both steadily increase with depth downcore (Fig. 21), most likely reflecting cation exchange reactions involved with authigenic clay formation.

High-Resolution Study Targeting the Potential Presence of Methane Hydrate

The presence of methane hydrate in sedimentary sequences is easily documented by interstitial water chemistry because the decomposition of the hydrate during recovery sharply decreases salinity and

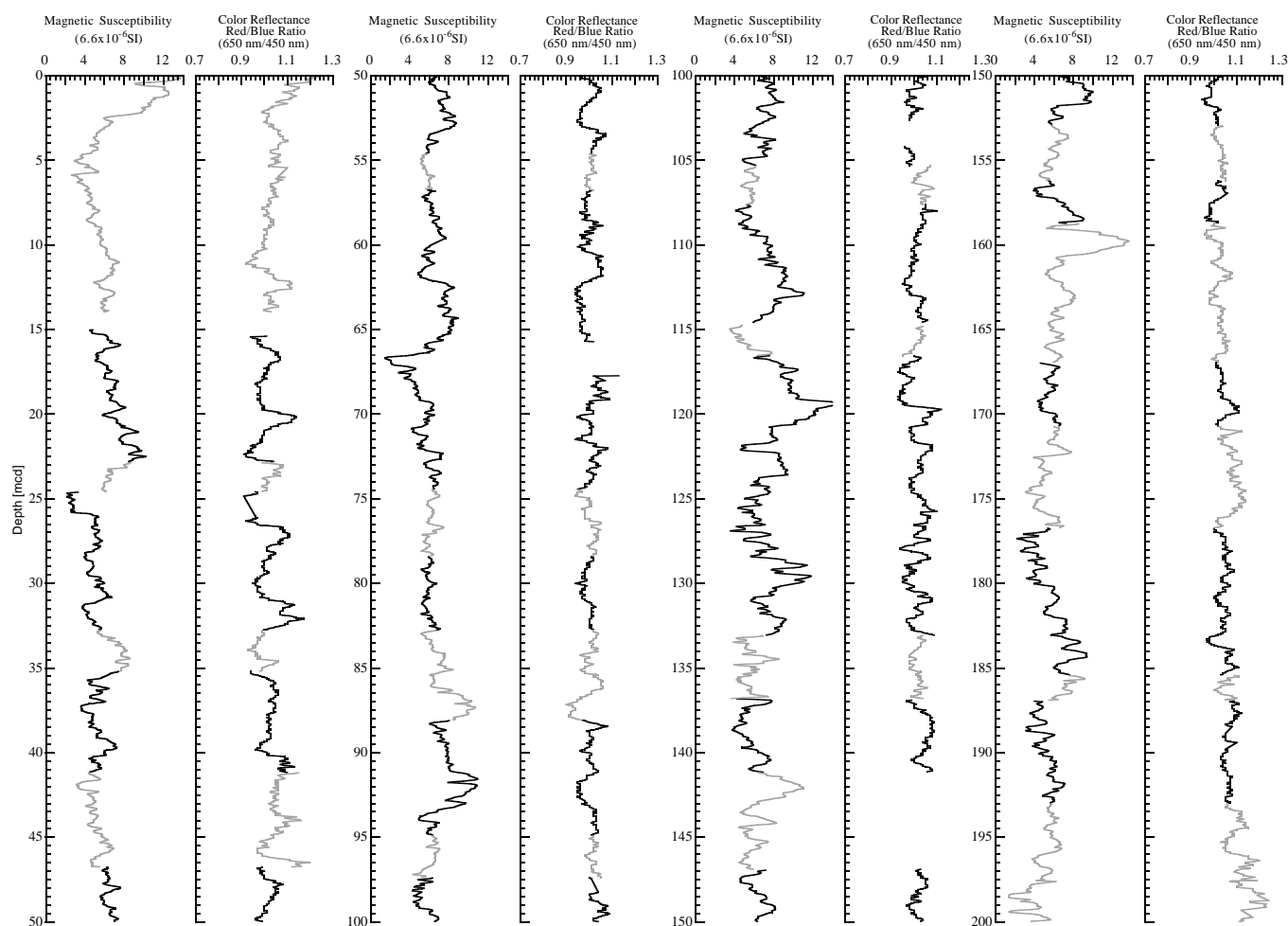


Figure 16. Spliced records for magnetic susceptibility and color reflectance (red/blue ratio [650 nm/450 nm]) plotted in meters composite depth (mcd). Cores from Holes 1077A and 1077B have been used for the spliced record: black line = Hole 1077A and gray line = Hole 1077B.

dissolved Cl^- concentrations. At Site 1077, salinity steadily decreases downcore, whereas the concentration of dissolved Cl^- increases relatively smoothly (Fig. 22). Neither of these profiles is characteristic of hydrate presence in the sedimentary sequence. The depth interval that was highlighted by seismic stratigraphic studies (see “Site Geophysics” section, “Site 1075” chapter, this volume) as a zone potentially bearing methane hydrate yielded no chemical evidence of the presence of methane hydrate, nor did any other portion of the sequence recovered from Site 1077.

ORGANIC GEOCHEMISTRY

Calcium carbonate and organic carbon concentrations were measured on sediment samples from Hole 1077A (Table 11). Organic matter atomic carbon/nitrogen (C/N) ratios and Rock-Eval pyrolysis analyses were employed to determine the type of organic matter contained within the sediments. High gas contents were encountered, and routine monitoring of the sedimentary gases was done for drilling safety.

Inorganic and Organic Carbon Concentrations

Concentrations of carbonate carbon are low in Site 1077 sediments. They vary between 1.6 and 0.1 wt% (Table 11). The maximum carbonate carbon concentration is equivalent to 13.3 wt% sedimentary CaCO_3 . These generally low concentrations agree with the

paucity of coccoliths and other calcareous microfossils in these hemipelagic sediments (see “Biostratigraphy and Sedimentation Rates” section, this chapter). The range in concentrations reflects a varying combination of changes in biological production of calcareous material, dilution by noncalcareous components, and carbonate dissolution fueled by oxidation of organic matter.

TOC determinations were done on a smaller number of Hole 1077A sediment samples than carbonate determinations because of the generally uniform lithology. TOC values range from 4.70 to 1.29 wt% (Table 11) and average 2.30 wt%. The concentrations are nearly 10 times greater than the average of 0.3 wt% given by McIver (1975) based Deep Sea Drilling Project (DSDP) Legs 1–33, a value that can be considered representative of typical deep-sea sediments. The high TOC concentrations at this site may be ascribed to a combination of a high supply of organic matter from elevated paleoproductivities and a high accumulation rate of sediments enhancing preservation of the organic matter.

Organic Matter Source Characterization

Organic C/N ratios were calculated for Site 1077 samples using TOC and total nitrogen concentrations to help identify the origin of their organic matter. Site 1077 C/N ratios vary from 14.5 to 10.6 (Table 11). The C/N ratios average 13.0, a value that is intermediate between unaltered algal organic matter (5–8) and fresh land-plant material (25–35; e.g., Emerson and Hedges, 1988; Meyers, 1994). It is likely that these organic carbon-rich sediments contain a mixture

Site 1077 Offsets

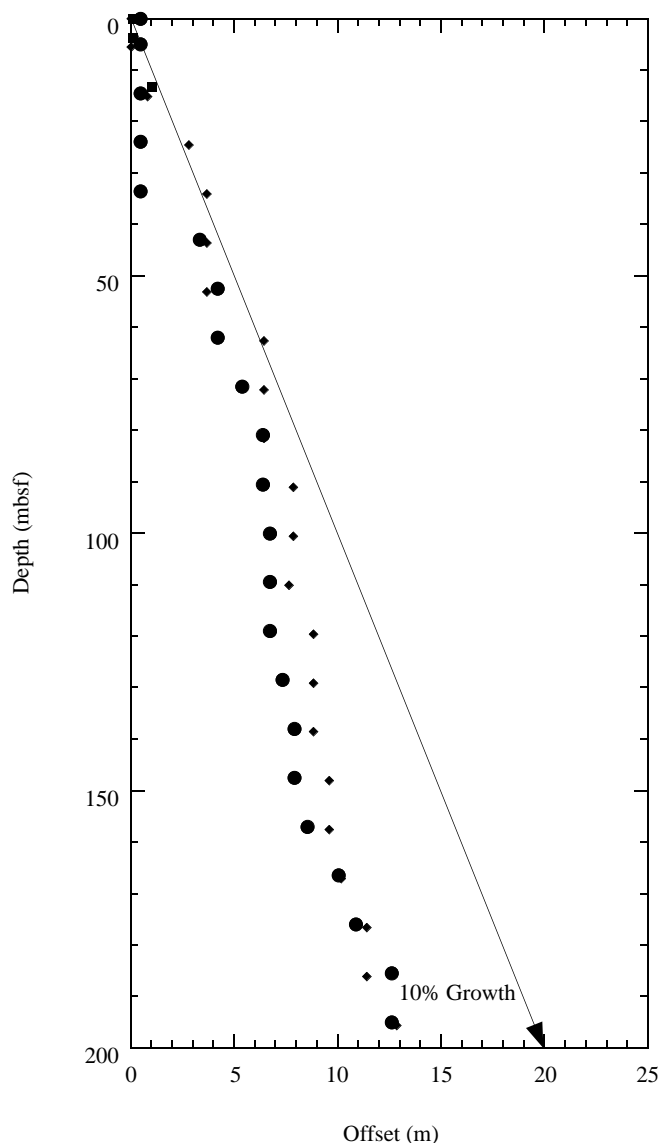


Figure 17. Core offsets applied to Site 1077 plotted against standard ODP meters below seafloor (mbsf). A linear 10% growth of meters composite depth (mcd) compared with mbsf is indicated by an arrow. Offsets are plotted for Holes 1077A (circles), 1077B (diamonds), and 1077C (squares).

of partially degraded algal material and detrital continental organic matter. Preferential loss of nitrogen-rich, proteinaceous matter can elevate the C/N ratios of algal organic matter during settling to the seafloor (Meyers, 1997).

Rock-Eval hydrogen index (HI) and oxygen index (OI) values indicate that Hole 1077A sediments contain a mixture of type II (algal) and type III (land-derived) organic matter (Table 12). This source assignment for the organic matter is consistent with the intermediate C/N ratios for these samples, which also suggest that the organic matter is a mixture of marine and continental material. An equally likely possibility, however, is that the sediments principally contain algal-derived organic matter that has been altered by microbial processing during early diagenesis. Well-preserved type II organic matter has high HI values (Peters, 1986), which can be lowered by microbial oxidation (Meyers, 1997). The low HI values of fresh type III organic

Table 8. Offsets applied to cores from Holes 1077A, 1077B, and 1077C.

Core	Depth (mbsf)	Offset (m)	Composite depth (mcd)
175-1077A-			
1H	0.0	0.44	0.44
2H	5.0	0.44	5.44
3H	14.5	0.44	14.94
4H	24.0	0.44	24.44
5H	33.5	0.44	33.94
6H	43.0	3.32	46.32
7H	52.5	4.20	56.70
8H	62.0	4.20	66.20
9H	71.5	5.38	76.88
10H	81.0	6.38	87.38
11H	90.5	6.38	96.88
12H	100.0	6.72	106.72
13H	109.5	6.72	116.22
14H	119.0	6.72	125.72
15H	128.5	7.32	135.82
16H	138.0	7.90	145.90
17H	147.5	7.90	155.40
18H	157.0	8.54	165.54
19H	166.5	10.04	176.54
20H	176.0	10.88	186.88
21H	185.5	12.62	198.12
22H	195.0	12.62	207.62
175-1077B-			
1H	0.0	0.00	0.00
2H	5.6	0.00	5.60
3H	15.1	0.80	15.90
4H	24.6	2.80	27.40
5H	34.1	3.66	37.76
6H	43.6	3.66	47.26
7H	53.1	3.66	56.76
8H	62.6	6.44	69.04
9H	72.1	6.44	78.54
10H	81.6	6.44	88.04
11H	91.1	7.84	98.94
12H	100.6	7.84	108.44
13H	110.1	7.66	117.76
14H	119.6	8.84	128.44
15H	129.1	8.84	137.94
16H	138.6	8.84	147.44
17H	148.1	9.60	157.70
18H	157.6	9.60	167.20
19H	167.1	10.16	177.26
20H	176.6	11.40	188.00
21H	186.1	11.40	197.50
22H	195.6	12.86	208.46
175-1077C-			
1H	0.0	0.00	0.00
2H	3.8	0.00	3.80
3H	13.3	0.80	14.10

Note: The offsets transform ODP standard depth values in meters below seafloor (mbsf) to meters composite depth (mcd).

matter, however, cannot become elevated by postdepositional alteration. In general, sediments having higher TOC values also have higher HI values (Table 12). This relationship implies that the algal organic matter has been oxidized. Further evidence of substantial amounts of in situ organic matter degradation exists in the large increases in alkalinity and decreases in sulfate in the interstitial waters of Site 1077 sediments (see "Inorganic Geochemistry" section, this chapter).

The elevated T_{max} value of Sample 175-1077A-1H-2, 0–5 cm (Table 12), reflects its poorly defined S_2 peak, not the actual thermal maturity of its organic matter. Most samples have relatively low T_{max} values, showing that organic matter is thermally immature with respect to petroleum generation (Peters, 1986) and therefore contains little detrital organic matter derived from the erosion of ancient sediments and transported to this site by the Congo River.

Headspace Gases

Sediments from Site 1077 had high gas content. Gas pressures became great enough in sediments below Core 175-1077A-10H (81 mbsf) to require perforating the core liner to relieve the pressure and

Table 9. List of splice tie points used to create the continuous “spliced” stratigraphic sequence for Site 1077.

Hole, core, section, interval (cm)	Depth (mbsf)	Composite depth (mcd)	Whether tied	Hole, core, section, interval (cm)	Depth (mbsf)	Composite depth (mcd)	Offset (m)
1077B-1H-4, 92	5.42	5.42	Tie to	1077B-2H-1, 0	5.60	5.60	0.00
1077B-2H-6, 84	13.94	13.94	Tie to	1077A-3H-1, 0	14.50	14.94	0.44
1077A-3H-6, 38	22.38	22.82	Tie to	1077B-3H-5, 92	22.02	22.82	0.80
1077B-3H-6, 118	23.78	24.58	Tie to	1077A-4H-1, 14	24.14	24.58	0.44
1077A-4H-6, 82	32.32	32.76	Tie to	1077B-4H-4, 86	29.96	32.76	2.80
1077B-4H-6, 28	32.38	35.18	Tie to	1077A-5H-1, 124	34.74	35.18	0.44
1077A-5H-5, 124	40.74	41.18	Tie to	1077B-5H-3, 42	37.52	41.18	3.66
1077B-5H-6, 148	43.08	46.74	Tie to	1077A-6H-1, 42	43.42	46.74	3.32
1077A-6H-6, 76	51.26	54.58	Tie to	1077B-6H-5, 132	50.92	54.58	3.66
1077B-6H-7, 54	53.14	56.80	Tie to	1077A-7H-1, 0	52.50	56.70	4.20
1077A-7H-7, 62	62.16	66.36	Tie to	1077B-8H-1, 16	62.16	66.36	4.20
1077A-8H-6, 72	70.22	74.42	Tie to	1077B-8H-4, 88	67.98	74.42	6.44
1077B-8H-7, 32	71.92	78.36	Tie to	1077A-9H-1, 148	72.98	78.36	5.38
1077A-9H-4, 138	77.38	82.76	Tie to	1077B-9H-3, 121	76.32	82.76	6.44
1077B-9H-7, 52	81.62	88.06	Tie to	1077A-10H-1, 68	81.68	88.06	6.38
1077A-10H-6, 60	88.50	94.88	Tie to	1077B-10H-5, 84	88.44	94.88	6.44
1077B-10H-7, 32	90.92	97.36	Tie to	1077A-11H-1, 48	90.98	97.36	6.38
1077A-11H-6, 112	98.92	105.30	Tie to	1077B-11H-5, 36	97.46	105.30	7.84
1077B-11H-6, 116	99.76	107.60	Tie to	1077A-12H-1, 88	100.88	107.60	6.72
1077A-12H-6, 36	107.86	114.58	Tie to	1077B-12H-4, 139	106.74	114.58	7.84
1077B-12H-6, 28	108.69	116.53	Tie to	1077A-13H-1, 30.5	109.81	116.53	6.72
1077A-13H-7, 52	119.02	125.74	Tie to	1077B-14H-1, 0	119.00	125.72	6.72
1077A-14H-5, 144	126.34	133.06	Tie to	1077B-14H-5, 2.5	124.22	133.06	8.84
1077B-14H-7, 84	127.97	136.81	Tie to	1077A-15H-1, 98.5	129.49	136.81	7.32
1077A-15H-4, 84	133.84	141.16	Tie to	1077B-15H-3, 21	132.32	141.16	8.84
1077B-15H-7, 36	138.06	146.90	Tie to	1077A-16H-1, 100	139.00	146.90	7.90
1077A-16H-5, 100	145.00	152.90	Tie to	1077B-16H-4, 96	144.06	152.90	8.84
1077B-16H-6, 124	147.34	156.18	Tie to	1077A-17H-1, 77	148.28	156.18	7.90
1077A-17H-3, 32	150.82	158.72	Tie to	1077B-17H-1, 101	149.12	158.72	9.60
1077B-17H-7, 24	157.34	166.94	Tie to	1077A-18H-1, 140	158.40	166.94	8.54
1077A-18H-4, 66	162.16	170.70	Tie to	1077B-18H-3, 49	161.10	170.70	9.60
1077B-18H-7, 52	167.12	176.72	Tie to	1077A-19H-1, 17	166.68	176.72	10.04
1077A-19H-6, 136	175.36	185.40	Tie to	1077B-19H-6, 64	175.24	185.40	10.16
1077B-19H-7, 64	176.74	186.90	Tie to	1077A-20H-1, 0	176.00	186.88	10.88
1077A-20H-5, 20	182.10	192.98	Tie to	1077B-20H-4, 48	181.58	192.98	11.40
1077B-20H-7, 56	186.16	197.56	Tie to	1077A-21H-1, 0	186.10	197.50	11.40
1077B-21H-6, 28	193.88	205.28	Tie to	1077A-21H-5, 116	192.66	205.28	12.62
1077A-21H-7, 64	195.14	207.76	Tie to	1077A-22H-1, 13	195.14	207.76	12.62
1077A-22H-3, 48	198.48	211.10	Tie to	1077B-22H-2, 113	198.24	211.10	12.86
1077B-22H-7, 64	205.24	218.10					

Note: The tie points are listed in standard ODP meters below seafloor (mbsf) and meters composite depth (mcd).

Table 10. Interstitial water composition for Holes 1077A and 1077B.

Core, section, interval (cm)	Depth (mbsf)	pH	Alkalinity (mM)	Salinity	Cl ⁻ (titr) (mM)	Cl ⁻ (IC) (mM)	SO ₄ ²⁻ (mM)	Na ⁺ (mM)	Mg ²⁺ (mM)	Ca ²⁺ (mM)	K ⁺ (mM)	H ₄ SiO ₄ (μM)	NH ₄ ⁺ (μM)	PO ₄ ³⁻ (μM)	Sr ²⁺ (μM)
175-1077A-															
1H-1, 140-150	1.50	7.67	4.240	35.5	560	553	27.22	481	51.82	10.84	12.51	549	262	16	93
1H-3, 140-150	4.50	7.53	4.720	35.5	559	552	26.70	480	51.62	10.78	12.46	703	407	21	94
2H-3, 140-150	9.50	7.71	16.279	35.5	561	551	18.67	487	48.96	8.86	11.73	699	1394	115	98
3H-3, 140-150	19.00	7.78	31.424	34.5	562	558	3.52	483	46.66	6.17	11.97	712	2350	244	111
4H-3, 140-150	28.50	7.26	34.537	35.0	563	556	0.67	484	46.29	5.02	11.89	794	2611	148	124
5H-3, 140-150	38.00	7.39	36.025	34.5	564	560	0.15	486	46.22	4.70	12.37	784	3101	98	128
6H-3, 140-150	47.50	7.46	34.903	34.5	565	556	0.00	486	45.58	4.82	12.76	784	3287	126	127
7H-3, 140-150	57.00	7.40	35.885	34.5	562	553	0.04	486	45.10	4.90	12.78	805	3459	110	126
8H-3, 140-150	66.50	7.51	33.094	34.5	566	558	0.00	488	44.31	5.04	12.94	827	3983	124	126
9H-3, 140-150	76.00	7.41	36.620	34.0	564	556	0.65	493	42.84	5.11	13.28	820	4010	99	125
10H-3, 120-130	85.10	7.56	34.644	34.0	565	556	0.00	490	42.44	5.38	14.12	760	4003	103	127
11H-3, 120-130	94.80	7.49	32.985	34.0	561	556	0.26	489	41.13	4.85	13.59	792	4416	96	126
14H-3, 130-140	123.40	7.72	28.124	33.5	563	563	0.04	494	36.77	4.50	14.62	723	5229	38	128
17H-3, 130-140	151.90	7.52	30.689	33.5	563	560	0.10	500	35.16	5.00	13.64	898	5533	39	136
20H-2, 130-140	178.90	7.29	30.904	33.5	566	562	0.00	504	34.39	5.73	13.30	963	5105	51	139
22H-6, 130-140	203.90	7.44	31.237	33.5	568	563	0.54	509	32.89	5.88	13.69	983	6249	42	139
175-1077B-															
12H-2, 150-160	103.74	7.55	32.384	34.5	566	557	0.41	498	39.33	4.54	12.98	917	4554	61	128
12H-4, 147-157	106.85	7.58	31.313	34.0	564	563	0.00	493	40.14	4.65	12.47	1030	4830	126	131
12H-6, 151-161	110.02	7.48	30.753	34.0	565	558	0.17	496	38.78	4.58	14.14	840	5071	70	127
13H-2, 134-154	112.94	7.80	29.788	34.0	564	560	0.13	492	39.21	4.89	13.44	991	4740	68	129
13H-4, 131-151	115.91	7.90	32.569	34.0	563	558	0.52	497	38.38	4.76	13.32	1011	4899	83	130
13H-6, 138-158	118.95	7.94	32.436	34.0	566	562	0.00	499	38.00	4.76	13.72	972	5099	78	131
14H-2, 122-132	122.30	7.86	31.377	34.0	563	559	0.52	496	38.20	4.80	13.47	977	5057	74	128
14H-4, 130-150	125.21	7.99	31.327	34.0	568	558	0.38	500	38.10	4.92	13.61	974	5229	66	131
14H-6, 145-155	128.18	7.93	31.051	34.0	566	556	0.00	500	36.57	4.67	15.00	902	5264	33	131

Note: Cl⁻ (titr) = analyzed by titration and Cl⁻ (IC) = analyzed by ion chromatography.

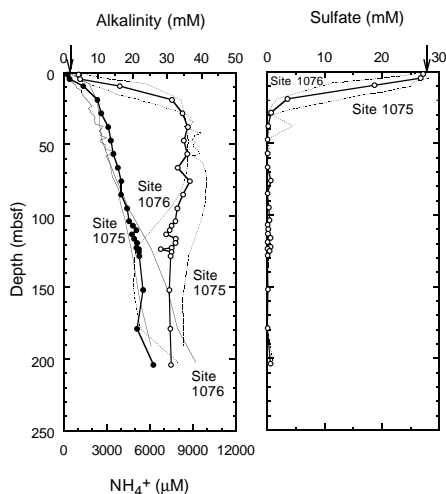


Figure 18. Downcore profiles of dissolved alkalinity (open circles), ammonium (solid circles), and sulfate (right panel) at Site 1077. Arrows = mean ocean-bottom-water values taken from Millero and Sohn (1992). For comparison, profiles for Sites 1075 and 1076 are also shown (as labeled).

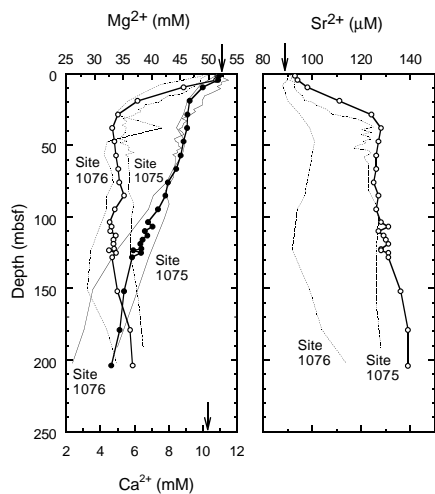


Figure 19. Downcore profiles of Ca^{2+} (open circles), Mg^{2+} (solid circles), and Sr^{2+} (right panel) at Site 1077. Arrows = mean ocean-bottom-water values taken from Millero and Sohn (1992). For comparison, profiles for Sites 1075 and 1076 are also shown (as labeled).

alleviate core expansion. Natural gas analyses determined that much of this gas was CO_2 (Table 13). Hydrogen sulfide could be detected by nose, but not by hydrogen sulfide-sensing instruments having a sensitivity of ~ 1 ppm, in Cores 175-1077A-2H through 4H (5–33.5 mbsf).

Methane (C_1) first appears in headspace gas samples in Hole 1077A sediments at 4.5 mbsf. Concentrations gradually increase and become significant in sediments below 28 mbsf (Fig. 23). As at Sites 1075 and 1076, high methane/ethane (C_1/C_2) ratios and the absence of major contributions of higher molecular weight hydrocarbon gases (Table 13) indicate that the gas is biogenic, as opposed to thermogenic, in origin. A biogenic origin of the methane is supported by the disappearance of interstitial sulfate at approximately the same sub-bottom depth where methane concentrations begin to rise (see “Inor-

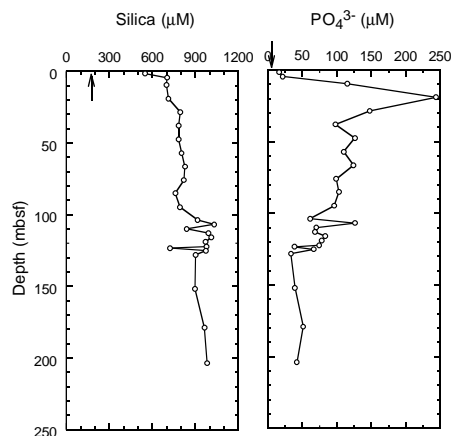


Figure 20. Downcore profiles of dissolved silica and phosphate at Site 1077. Arrows = mean ocean-bottom-water values taken from Millero and Sohn (1992).

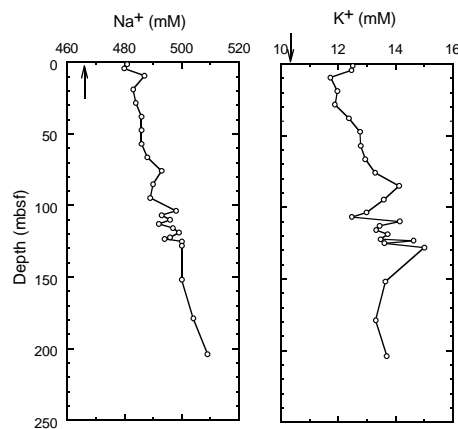


Figure 21. Downcore profiles of dissolved Na^+ and K^+ at Site 1077. Arrows = mean ocean-bottom water values taken from Millero and Sohn (1992).

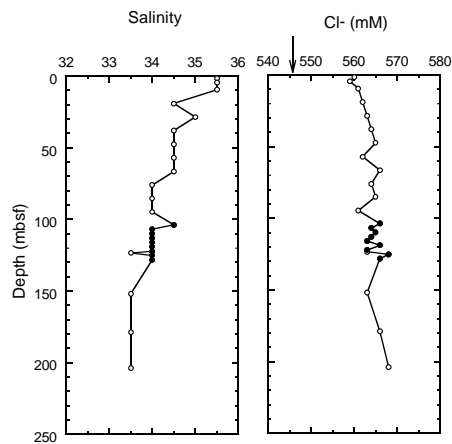


Figure 22. Downcore profiles of salinity and dissolved Cl^- at Site 1077. Solid symbols = high-resolution study for Hole 1077B. Arrow = mean ocean-bottom-water value taken from Millero and Sohn (1992).

Table 11. Percentages of inorganic and total carbon, total nitrogen, and total sulfur in sediment samples from Hole 1077A.

Core, section, interval (cm)	Depth (mbsf)	IC (wt%)	CaCO ₃ (wt%)	TC (wt%)	TOC (wt%)	TN (wt%)	TS (wt%)	C/N (atomic)
175-1077A-								
1H-1W, 46-47	0.46	0.11	0.94					
1H-2W, 0-5	1.50	0.26	2.12	2.40	2.14	0.17	0.82	14.4
1H-3W, 145-150	3.00	0.48	4.02	3.10	2.62	0.23	1.05	13.5
1H-3W, 46-47	3.46	0.48	4.03					
2H-1W, 46-47	5.46	0.14	1.16					
2H-3W, 46-47	8.46	0.21	1.71					
2H-4W, 0-5	9.50	0.17	1.41	2.58	2.41	0.19	1.10	14.7
3H-1W, 46-47	14.96	0.13	1.12					
3H-3W, 46-47	17.96	0.19	1.58					
3H-4W, 0-5	19.00	0.11	0.88	2.05	1.95	0.17	0.66	13.6
3H-5W, 46-47	20.96	0.24	2.03					
4H-2W, 46-47	25.96	0.63	5.24					
4H-4W, 0-5	28.50	0.20	1.64	2.66	2.47	0.20	1.52	14.1
4H-4W, 46-47	28.96	0.29	2.43					
4H-6W, 46-47	31.96	0.11	0.92					
5H-1W, 46-47	33.96	0.13	1.04					
5H-3W, 46-47	36.96	0.24	1.96					
5H-4W, 0-5	38.00	0.32	2.63	3.58	3.27	0.26	1.78	14.5
5H-5W, 46-47	39.96	1.17	9.75					
6H-1W, 46-47	43.46	0.43	3.54					
6H-3W, 46-47	46.46	0.19	1.59					
6H-4W, 0-5	47.50	0.10	0.83	4.80	4.70	0.38	1.75	14.4
6H-5W, 46-47	49.46	0.36	2.98					
7H-1W, 46-47	52.96	0.35	2.89					
7H-3W, 46-47	55.96	0.25	2.04					
7H-4W, 0-5	57.04	0.22	1.84	3.70	3.48	0.31	2.21	13.1
7H-5W, 46-47	59.00	0.15	1.25					
8H-3W, 46-47	65.46	1.12	9.31					
8H-4W, 0-5	66.50	0.57	4.71	2.89	2.33	0.20	2.00	13.6
8H-5W, 46-47	68.46	0.17	1.41					
9H-1W, 46-47	71.96	0.16	1.30					
9H-3W, 46-47	74.96	0.39	3.22					
9H-4W, 0-5	76.00	0.76	6.37	3.36	2.59	0.22	1.75	14.1
9H-5W, 46-47	77.96	0.14	1.19					
10H-1W, 46-47	81.46	0.21	1.77					
10H-3W, 46-47	84.26	0.15	1.24					
10H-4W, 0-5	85.10	0.10	0.81	2.16	2.07	0.19	2.14	12.9
10H-5W, 46-47	86.86	0.59	4.91					
11H-1W, 46-47	90.96	0.25	2.11					
11H-3W, 46-47	93.96	0.16	1.35					
11H-4W, 0-5	94.80	0.15	1.21	1.43	1.29	0.14	2.42	10.6
11H-5W, 46-47	96.76	0.42	3.50					
12H-1W, 46-47	100.46	0.67	5.61					
12H-3W, 46-47	103.46	0.18	1.54					
12H-5W, 46-47	106.46	1.04	8.64					
12H-7W, 0-5	109.00	0.25	2.07	3.12	2.88	0.24	2.46	14.2
13H-1W, 46-47	109.96	0.42	3.47	2.67	2.26	0.19	2.08	13.6
13H-3W, 22-23	112.72	0.68	5.63	2.19	1.51	0.16	0.97	11.4
13H-3W, 46-47	112.96	1.58	13.18	3.91	2.33	0.22	2.17	12.5
13H-3W, 60-61	113.10	1.59	13.26	4.07	2.48	0.23	3.13	12.4
13H-3W, 113-114	113.63	0.68	5.69	3.08	2.40	0.20	2.17	14.4
13H-5W, 46-47	115.96	0.25	2.07	1.59	1.34	0.14	1.03	11.1
13H-7W, 0-5	118.50	0.36	2.96	1.91	1.55	0.16	2.30	11.5
14H-1W, 46-47	119.46	0.13	1.05					
14H-3W, 46-47	122.46	0.47	3.90					
14H-4W, 0-5	123.40	0.12	1.02	2.03	1.90	0.17	2.04	13.3
14H-5W, 46-47	125.36	0.07	0.61					
15H-1W, 50-51	129.00	0.13	1.08					
15H-3W, 46-47	131.96	0.19	1.56					
15H-5W, 46-47	134.96	0.23	1.89					
15H-7W, 0-5	137.50	0.10	0.86	1.80	1.70	0.16	2.10	12.3
16H-1W, 46-47	138.46	0.40	3.36					
16H-3W, 46-47	141.46	0.19	1.55					
16H-5W, 46-47	144.46	0.30	2.46					
16H-7W, 0-5	147.00	0.37	3.11	3.00	2.63	0.23	2.47	13.5
17H-1W, 46-47	147.96	0.38	3.16					
17H-3W, 46-47	150.96	0.58	4.82					
17H-4W, 0-5	151.90	0.71	5.93	2.67	1.96	0.20	2.37	11.7
17H-5W, 46-47	153.66	0.25	2.12					
18H-1W, 46-47	157.46	0.26	2.17					
18H-3W, 46-47	160.46	0.30	2.47					
18H-5W, 46-47	163.46	0.13	1.09					
18H-7W, 0-5	166.00	0.15	1.24	3.14	2.99	0.26	2.33	13.2
19H-1W, 46-47	166.96	0.27	2.21					
19H-3W, 46-47	169.96	0.18	1.52					
19H-5W, 46-47	172.96	0.18	1.48					
19H-7W, 0-5	175.50	0.18	1.51	1.59	1.41	0.15	1.40	10.8
20H-1W, 46-47	176.46	0.19	1.59					
20H-3W, 0-5	178.90	0.21	1.76	2.40	2.19	0.20	1.83	13.1
20H-3W, 46-47	179.36	0.30	2.54					
20H-5W, 46-47	182.36	0.34	2.83					
21H-1W, 46-47	185.96	0.20	1.63					
21H-3W, 46-47	188.96	0.24	1.97					
21H-5W, 46-47	191.96	0.21	1.75					
21H-7W, 0-5	194.50	0.20	1.67	2.04	1.84	0.17	2.40	12.7
22H-1W, 46-47	195.46	0.23	1.95					
22H-3W, 46-47	198.46	0.30	2.54					
22H-5W, 46-47	201.46	0.30	2.47					
22H-7W, 0-5	203.90	0.28	2.30	2.31	2.03	0.21	2.38	11.1

Notes: IC = inorganic carbon; CaCO₃ = calcium carbonate; TC = total carbon; TOC = total organic carbon; TN = total nitrogen; TS = total sulfur; and C/N = carbon/nitrogen ratio. TOC concentrations are calculated from the difference between IC and TC concentrations. C/N ratios are calculated from TOC and TN concentrations and are given as atom/atom ratios.

ganic Geochemistry” section, this chapter). As noted by Claypool and Kvenvolden (1983), the presence of interstitial sulfate inhibits methanogenesis in marine sediments.

Sampling of headspace gases was done at 3-m intervals between 100 and 130 mbsf at Hole 1077B to test for the presence of methane hydrates that might be responsible for a conspicuous seismic reflector seen at this level. No evidence of extraordinary amounts of methane was found (Table 13).

PHYSICAL PROPERTIES

MST measurements were conducted on whole-round sections of cores from each hole to obtain wet bulk density, compressional (*P*-wave) ultrasonic velocity, and magnetic susceptibility (see “Explanatory Notes” chapter, this volume). Natural gamma radiation was measured below 75 mbsf for a comparison with results from in situ logging (see “Downhole Logging” section, this chapter). Similar to Site 1076, many core sections from this site showed mechanical disturbance, probably because of degassing processes during core retrieval (see “Lithostratigraphy” section, this chapter).

Index properties (gravimetric density) measurements were made on one or two samples (volume = ~10 cm³) per working-half section on all cores (see “Explanatory Notes” chapter, this volume). Method C was utilized at this site.

Ultrasonic compressional (*P*-wave) velocities and undrained vane-shear measurements were made at a resolution of one or two samples per section. For the discrete *P*-wave pulse-transmission experiments, the digital sediment velocimeter (DSV) and the modified Hamilton Frame transducer systems were used.

Multisensor Track

The sampling rate for ultrasonic compressional wave velocity, GRAPE density (Fig. 24), and magnetic susceptibility (Fig. 25A) was 2 cm for the upper 75 m and was changed to 4 cm below 75 mbsf. MST data are included on CD-ROM (back pocket, this volume). At this depth, natural gamma radiation measurements were incorporated in the MST measurements, with a sampling period of 30 s at 4-cm resolution (Fig. 25B). Magnetic susceptibility and natural gamma radiation show some similarity in their profiles (Fig. 25A and B, respectively), which may be attributed to higher proportions of magnetic particles at higher clay contents primarily monitored with NGR measurements (see “Lithostratigraphy” and “Downhole Logging” sections, this chapter). GRAPE density shows a good general correlation with discrete wet bulk density data (Fig. 24A–D). All MST core logs reveal pronounced cycles in physical properties and will, after thorough editing, provide high-resolution proxy information for

Table 12. Results of Rock-Eval pyrolysis analyses of sediments from Hole 1077A.

Core, section, interval (cm)	Depth (mbsf)	TOC (wt%)	S ₁	S ₂	S ₃	T _{max} (°C)	HI	OI
175-1077A-1H-2, 0-5	1.50	2.14	0.39	4.40	5.02	491	205	234
6H-4, 0-5	47.50	4.70	0.96	13.27	5.58	421	284	118
12H-7, 0-5	109.00	2.88	0.44	5.22	4.82	413	181	167
17H-4, 0-5	151.90	1.96	0.34	2.98	4.88	411	152	248
22H-7, 0-5	203.90	2.03	0.71	5.09	3.39	405	250	166

Notes: TOC = total organic carbon; HI = hydrogen index; and OI = oxygen index. Units of the various Rock-Eval parameters are given in the “Organic Geochemistry” section of the “Explanatory Notes” chapter (this volume).

Table 13. Results of headspace gas analyses of sediments from Holes 1077A and 1077B.

Core, section, interval (cm)	Depth (mbsf)	C ₁ (ppmv)	CO ₂ (ppmv)	C ₂ = (ppmv)	C ₂ (ppmv)	C ₃ = (ppmv)	C ₃ (ppmv)	C ₁ /C ₂
175-1077A-1H-2, 0-5	1.50	6	1,011					
1H-3, 145-150	3.00	9.6						
2H-4, 0-5	9.50	102			0.2		510	
3H-4, 0-5	28.50	334			0.3		1,113	
4H-4, 0-5	38.00	10,271	21,096		1.4		7,336	
5H-4, 0-5	47.50	18,458		0.2	1.9		9,715	
6H-4, 0-5	57.04	30,241		0.2	3.5		8,640	
7H-4, 0-5	66.50	54,717		0.2	5.8		9,434	
8H-4, 0-5	76.00	37,234	18,403	0.2	4.2		1	8,865
9H-4, 0-5	85.10	48,443		0.2	5.8		1	8,352
10H-4, 0-5	94.80	47,700		0.3	5.9		1	8,085
11H-4, 0-5	109.00	44,095		0.2	5.7		1	7,736
12H-7, 0-5	118.50	34,920	22,576	0.2	5.5		1	6,349
13H-7, 0-5	123.40	27,645		0.1	4.9		1	5,642
14H-4, 0-5	137.50	16,398		0.3	3.5			4,685
15H-7, 0-5	147.00	38,264		0.2	7.1		2	5,389
16H-7, 0-5	151.90	26,687	17,868	0.1	6.1	0.04	2	4,375
17H-4, 0-5	151.90	44,860		0.4	9.3		2	4,824
18H-7, 0-5	166.00	15,168		0.04	4.3	0.04	1	3,527
19H-7, 0-5	175.50	12,331	15,605	0.09	2.9		1	4,252
20H-3, 0-5	178.90	24,069		0.21	6.3		1	3,820
21H-7, 0-5	194.50	8,548			2.3		0	3,717
22H-7, 0-5	203.90	8,568	18,126	0.05	2.8		1	3,060
175-1077B-12H-3, 0-5	103.74	10,954	8,313	0.2	2.3			4,763
12H-5, 0-5	106.85	27,946		0.3	5.3			5,273
12H-7, 0-5	110.02	19,356		0.2	3.3			5,865
13H-3, 0-5	112.94	10,992	11,068	0.4	2.8		1	3,926
13H-5, 0-5	115.91	13,670		0.5	3.3		1	4,142
13H-7, 0-5	118.95	40,694	16,932	0.3	6.5		1	6,261
14H-3, 0-5	121.32	7,116		0.3	1.8		0	3,953
14H-5, 0-5	124.19	15,126		0.8	4.4		1	3,438
14H-7, 0-5	127.13	34,809	21,493	0.5	7.6		2	4,580

Notes: C₁ = methane; CO₂ = carbon dioxide; C₂= = ethene; C₂ = ethane; C₃= = propene; and C₃ = propane. Dominance of C₁ over C₂ indicates that the gases originate from in situ microbial degradation of organic matter.

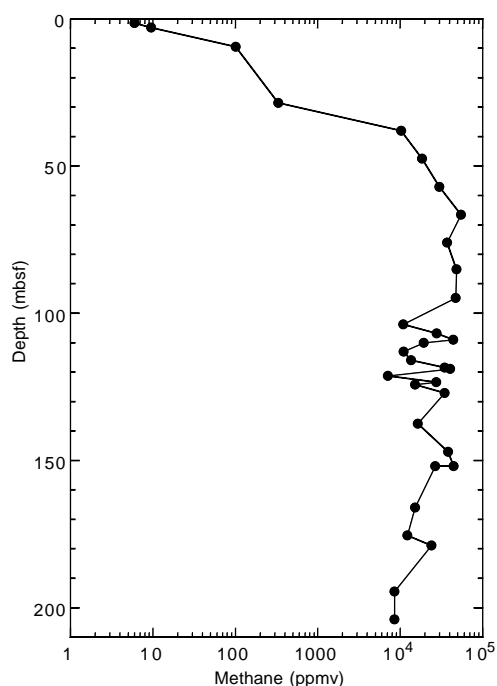


Figure 23. Headspace methane concentrations in sediments from Site 1077.

fast temporal changes of sediment composition and environmental conditions. Compressional velocities were disregarded because of instrumental problems with the MST *P*-wave sensors (see “Physical Properties” section, “Site 1076” chapter, this volume).

Velocities

Since the near-continuous velocity profile recorded with the MST had to be disregarded because of instrumental problems, only discrete velocity measurements are available. Velocities range between 1450 and 1555 m/s (Fig. 26). Discrete velocity measurements were conducted with the DSV system down to 35 mbsf, and then a switch was made to the Hamilton Frame (Fig. 26). The ultrasonic signals were highly attenuated below 100 mbsf. Discrete velocity values show larger scatter within the upper 35 m but reveal little variation below. The significant increase in velocities at 35 mbsf coincides with the change from the DSV to the Hamilton Frame system. This indicated that measurements with the DSV could not be carried out in this type of clay-rich sediment without affecting the mechanical integrity of the sediment between the transducers. Furthermore, only velocity measurements with the Hamilton Frame were made, also avoiding calibration problems between the two systems.

Index Properties

Results of discrete measurements of wet bulk density, porosity, and moisture content are presented in Figures 27A, 27B, and 27C, respectively (also see Table 14 on CD-ROM, back pocket, this vol-

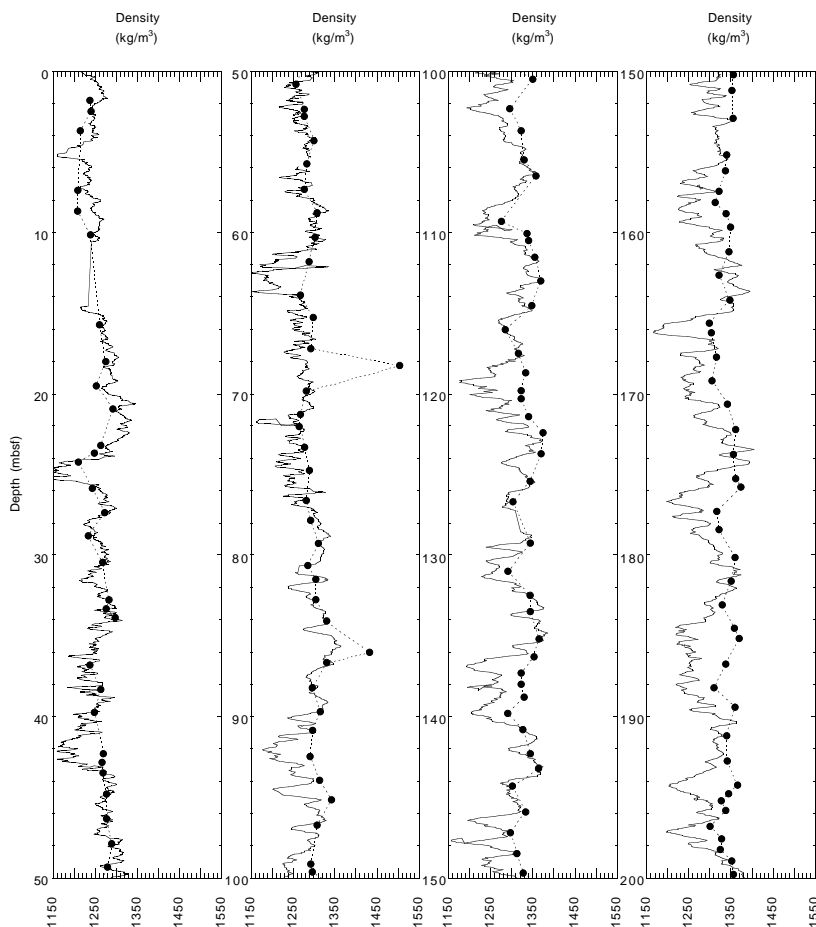


Figure 24. Discrete density values (solid circles) in comparison with the filtered and smoothed GRAPE density profile (solid line) at Hole 1077A.

ume). The density values vary within a narrow range between 1200 and 1350 kg/m³, indicating a very homogenous composition of the sediment (see “Lithostratigraphy” section, this chapter). A trend to higher values indicates compaction. Porosity decreases from 88% in the top section to 81% at 200 mbsf.

Thermal Conductivity and Geothermal Gradient

The thermal conductivity profile at Hole 1077A was measured by inserting a single probe in every second core section (see “Explanatory Notes” chapter, this volume). The values reveal significant scatter throughout the hole with decreasing values of even higher scatter toward the bottom (Fig. 25C).

In Hole 1077A, the Adara tool was deployed to measure formation temperature. A preliminary analysis provided five data points, which were used to estimate a geothermal gradient of 57°C/km, but further analyses will be required to confirm this result.

Vane Shear Strength

An undrained vane-shear measurement was performed in the bottom part of each core section. The profile shows a gradual increase of shear-strength values from the top to 115 mbsf (Fig. 25D). Because of the differential pressure that built up in the core liners during degassing, core integrity was more affected close to the top and bottom of each core. Accordingly, shear strength shows relative minima at the end of the cores. Maximum values probably represent undisturbed or less disturbed sections. From maximum values, an average increase in shear strength may be derived, which could be attributed to compaction.

DOWNHOLE LOGGING

Hole 1077A was logged with a limited suite of sensors to identify and locate the presence of gas hydrate in the sediments, to provide data for core-log integration, and to continuously characterize the sedimentary changes.

Logging Operations

Hole 1077A was logged to 202 mbsf with the seismostratigraphy logging tool string (25.8 m long) including the NGT, LSS, DITE-SFL, and LDEO-TLT sondes. The pipe was set at 75 mbsf, and the wireline heave compensator was started downhole at mudline. The log was run uphole at 400 m/hr from 202 mbsf (total depth) to pipe at 74 mbsf and then to seafloor. The natural gamma-ray intensity is the only parameter that is measurable through the pipe, but it can be interpreted only qualitatively in this interval.

Data Quality and General Results

The recorded data show only very fine-scale changes recorded by the sonic and electrical sensors (Fig. 28) caused by the high water content, which is the reason for a low acoustic velocity and a low electrical resistivity in the formation. The natural gamma-ray intensity given by the calculated gamma ray (CGR), mainly from potassium (K) and thorium (Th), is related to the clay concentration of the sediment. Consequently, the observed changes can be controlled by the detrital input, dilution by opal or carbonate, or a combination of both. CGR is positively correlated with electrical resistivity and negatively correlated with acoustic velocity. Clay-rich intervals corre-

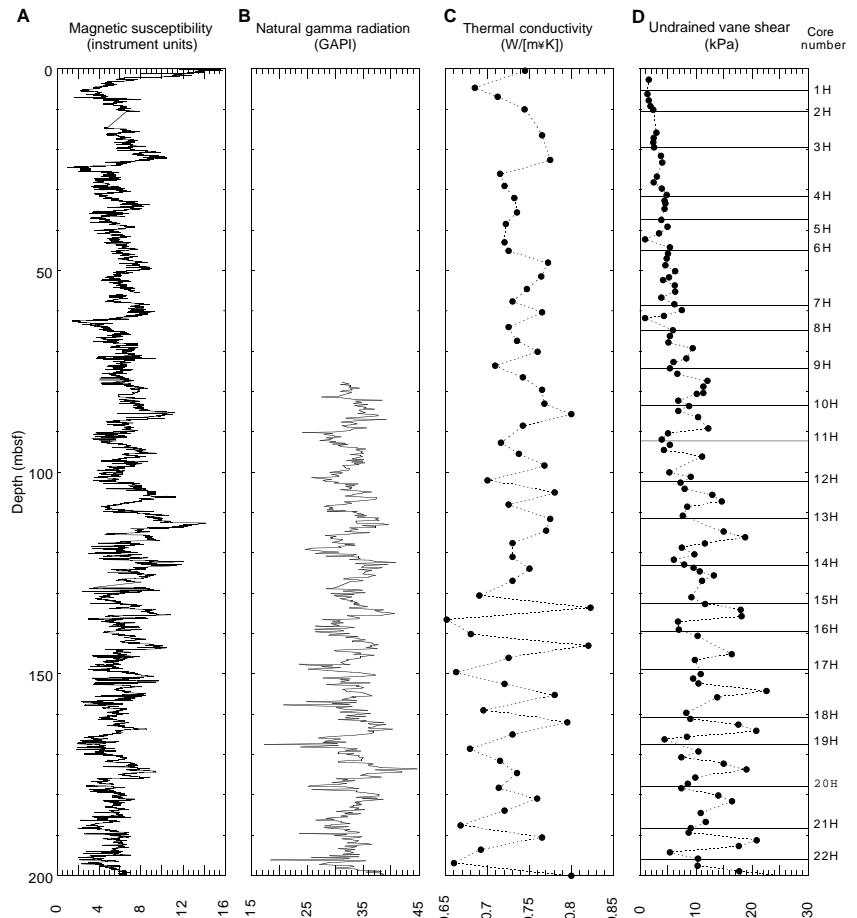


Figure 25. Plots of (A) magnetic susceptibility and (B) natural gamma radiation from MST measurements compared with discrete values of (C) thermal conductivity and (D) undrained vane-shear strength determinations at Hole 1077A.

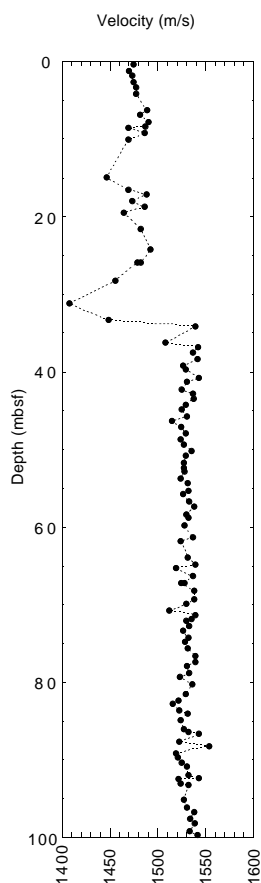


Figure 26. Discrete velocity profile measured down to 100 mbsf at Hole 1077A.

spond to high natural gamma radiation, high resistivity, and low acoustic velocity, whereas biogenic-rich intervals show the opposite trend. This pattern is well known for sediment dominated by siliceous biogenic components. The acoustic velocity exhibits a general trend through depth, with an increase downhole from 1460 to 1500 m/s. This might be caused by progressive compaction of the sediment with depth.

The spectral components (K, Th, and uranium [U]) of the natural gamma log show that the U content is low (1.5–3.5 ppm). Uranium enrichment commonly is associated with the presence of organic material (negative correlation with Th and K). In contrast, K (0.001%–0.009%) and Th (3–7 ppm) are carried by clays and peak in clay-rich intervals.

The temperature tool measures borehole fluid temperature, which can be used to estimate downhole thermal gradients provided that the data reflect borehole, rather than in situ formation, temperature. The results (Fig. 29) suggest a downhole thermal gradient of 25°C/km, although this is an underestimate because of the cooling effect of circulation during drilling. In situ temperature measurements using the Adara probe indicated a thermal gradient near 58°C/km at this site (see “Physical Properties” section, this chapter).

Log-Core Correlations

The core MST and log measurements of natural gamma-ray intensity show comparable large-scale variability in the lower part of the logged interval (Fig. 30), which would lead to similar depth scales for core and logging data. Core data are recorded in counts per second (cps), whereas log data are presented in API (Oil Industry Standard)

units. The core data appear noisier than the log data, despite having the same sampling resolution (about every 20 cm). The lower quality of the core measurements is most likely a result of core disturbance caused by gas expansion in conjunction with a short integration time. In the upper part of the hole, the correlation is not obvious, and comparisons between log and core data have to be made with caution.

REFERENCES

- Bé, A.W.H., and Tolderlund, D.S., 1971. Distribution and ecology of living planktonic foraminifera in surface waters of the Atlantic and Indian Oceans. In Funnel, B.M., and Riedel, W.R. (Eds.), *The Micropaleontology of Oceans*: Cambridge (Cambridge Univ. Press), 105–149.
- Berggren, W.A., Kent, D.V., Swisher, C.C., III, and Aubry, M.-P., 1995. A revised Cenozoic geochronology and chronostratigraphy. In Berggren, W.A., Kent, D.V., Aubry, M.-P., and Hardenbol, J. (Eds.), *Geochronology, Time Scales and Global Stratigraphic Correlation*. Spec. Publ.—Soc. Econ. Paleontol. Mineral. (Soc. Sediment. Geol.), 54:129–212.
- Claypool, G.E., and Kvenvolden, K.A., 1983. Methane and other hydrocarbon gases in marine sediment. *Annu. Rev. Earth Planet. Sci.*, 11:299–327.
- Curry, W.B., Shackleton, N.J., Richter, C., et al., 1995. *Proc. ODP, Init. Repts.*, 154: College Station, TX (Ocean Drilling Program).
- Emerson, S., and Hedges, J.I., 1988. Processes controlling the organic carbon content of open ocean sediments. *Paleoceanography*, 3:621–634.
- Fuller, M., and Garrett, E., in press. Site 395 appendix: magnetic experiments. In Becker, K., Malone, M.J., et al., *Proc. ODP, Init. Repts.*, 174B: College Station, TX (Ocean Drilling Program).
- Fuller, M., Hastedt, M., and Herr, B., 1997. Coring-induced magnetization of recovered sediment. In Weaver, P.P.E., Schmincke, H.-U., Firth, J.V., and Duffield, W. (Eds.), *Proc. ODP, Sci. Results*, 157: College Station, TX (Ocean Drilling Program), 47–56.
- Gartner, S., 1977. Calcareous nannofossil biostratigraphy and revised zonation of the Pleistocene. *Mar. Micropaleontol.*, 2:1–25.
- Imbrie, J., Hays, J.D., Martinson, D.G., McIntyre, A., Mix, A.C., Morley, J.J., Pisias, N.G., Prell, W.L., and Shackleton, N.J., 1984. The orbital theory of Pleistocene climate: support from a revised chronology of the marine $\delta^{18}\text{O}$ record. In Berger, A., Imbrie, J., Hays, J., Kukla, G., and Saltzman, B. (Eds.), *Milankovitch and Climate* (Pt. 1), NATO ASI Ser. C, Math Phys. Sci., 126:269–305.
- Jansen, J.H.F., Alderliesten, C., Houston, C.M., De Jong, A.F.M., Van der Borg, K., and Van Iperen, J.M., 1989. Aridity in equatorial Africa during the last 225,000 years: a record of opal phytoliths/freshwater diatoms from the Zaire (Congo) deep-sea fan (northeast Angola basin). *Radiocarbon*, 31:557–569.
- Jansen, J.H.F., Ufkes, E., and Schneider, R.R., 1996. Late Quaternary movements of the Angola-Benguela-Front, SE Atlantic, and implications for advection in the equatorial ocean. In Wefer, G., Berger, W.H., Siedler, G., and Webb, D. (Eds.), *The South Atlantic: Present and Past Circulation*: Berlin (Springer-Verlag), 553–575.
- Jansen, J.H.F., van Weering, T.G.E., Giesels, R., and van Iperen, J., 1984. Middle and late Quaternary oceanography and climatology of the Zaire-Congo fan and the adjacent eastern Angola Basin. *Neth. J. Sea Res.*, 17:201–241.
- Locker, S., 1996. Cenozoic siliceous flagellates from the Fram Strait and the East Greenland Margin: biostratigraphic and paleoceanographic results. In Thiede, J., Myhre, A.M., Firth, J.V., Johnson, G.L., and Ruddiman, W.F. (Eds.), *Proc. ODP, Sci. Results*, 151: College Station, TX (Ocean Drilling Program), 101–124.
- Martini, E., 1971. Standard Tertiary and Quaternary calcareous nannoplankton zonation. In Farinacci, A. (Ed.), *Proc. 2nd Int. Conf. Planktonic Microfossils Roma*: Rome (Ed. Tecnosci.), 2:739–785.
- McIver, R.D., 1975. Hydrocarbon occurrences from JOIDES Deep Sea Drilling Project. *Proc. Ninth Petrol. Congr.*, 269–280.
- Meyers, P.A., 1994. Preservation of elemental and isotopic source identification of sedimentary organic matter. *Chem. Geol.*, 144:289–302.
- , 1997. Organic geochemical proxies of paleoceanographic, paleolimnologic, and paleoclimatic processes. *Org. Geochem.*, 27:213–250.
- Millero, F.J., and Sohn, M.L., 1992. *Chemical Oceanography*: Boca Raton (CRC Press).
- Mix, A.C., and Morey, A.E., 1996. Climate feedback and Pleistocene variations in the Atlantic South Equatorial Current. In Wefer, G., Berger, W.H., Siedler, G., and Webb, D. (Eds.), *The South Atlantic: Present and Past Circulation*: Berlin (Springer-Verlag), 503–525.

- Mix, A.C., Rugh, W., Piasias, N.G., Veirs, S., Leg 138 Shipboard Sedimentologists (Hagelberg, T., Hovan, S., Kemp, A., Leinen, M., Levitan, M., Ravelo, C.), and Leg 138 Scientific Party, 1992. Color reflectance spectroscopy: a tool for rapid characterization of deep-sea sediments. *In* Mayer, L., Piasias, N., Janecek, T., et al., *Proc. ODP, Init. Repts.*, 138 (Pt. 1): College Station, TX (Ocean Drilling Program), 67–77.
- Moore, T.C., Jr., 1995. Radiolarian stratigraphy, Leg 138. *In* Piasias, N.G., Mayer, L.A., Janecek, T.R., Palmer-Julson, A., and van Andel, T.H. (Eds.), *Proc. ODP, Sci. Results*, 138: College Station, TX (Ocean Drilling Program), 191–232.
- Okada, H., and Bukry, D., 1980. Supplementary modification and introduction of code numbers to the low-latitude coccolith biostratigraphic zonation (Bukry, 1973; 1975). *Mar. Micropaleontol.*, 5:321–325.
- Peters, K.E., 1986. Guidelines for evaluating petroleum source rock using programmed pyrolysis. *AAPG Bull.*, 70:318–329.
- Shipboard Scientific Party, 1995. Site 926. *In* Curry, W.B., Shackleton, N.J., Richter, C., et al., *Proc. ODP, Init. Repts.*, 154: College Station, TX (Ocean Drilling Program), 153–232.
- , 1996. Explanatory notes. *In* Comas, M.C., Zahn, R., Klaus, A., et al., *Proc. ODP, Init. Repts.*, 161: College Station, TX (Ocean Drilling Program), 21–49.
- , 1998. Sites 1056, 1057, 1058, and 1059: Paleomagnetism. *In* Keigwin, L.D., Rio, D., Acton, G.D., et al., *Proc. ODP, Init. Repts.*, 172: College Station, TX (Ocean Drilling Program), 97–103.
- Singer, A., 1984. The paleoclimatic interpretation of clay minerals in sediments: a review. *Earth-Sci. Rev.*, 21:251–293.
- van der Gaast, S.J., and Jansen, J.H.F., 1984. Mineralogy, opal, and manganese of Middle and Late Quaternary sediments of the Zaire (Congo) deep-sea fan: origin and climatic variation. *Neth. J. Sea Res.*, 17:313–341.
- Weaver, P.P.E., 1993. High resolution stratigraphy of marine Quaternary sequences. *In* Hailwood, E.A., and Kidd, R.B. (Eds.), *High Resolution Stratigraphy*. Geol. Soc. Spec. Publ. London, 70:137–153.

Ms 1751R-105

NOTE: Core-description forms (“barrel sheets”) and core photographs can be found in Section 4, beginning on page 581. Forms containing smear-slide data and shore-based log processing data can be found on CD-ROM. See Table of Contents for materials contained on CD-ROM.

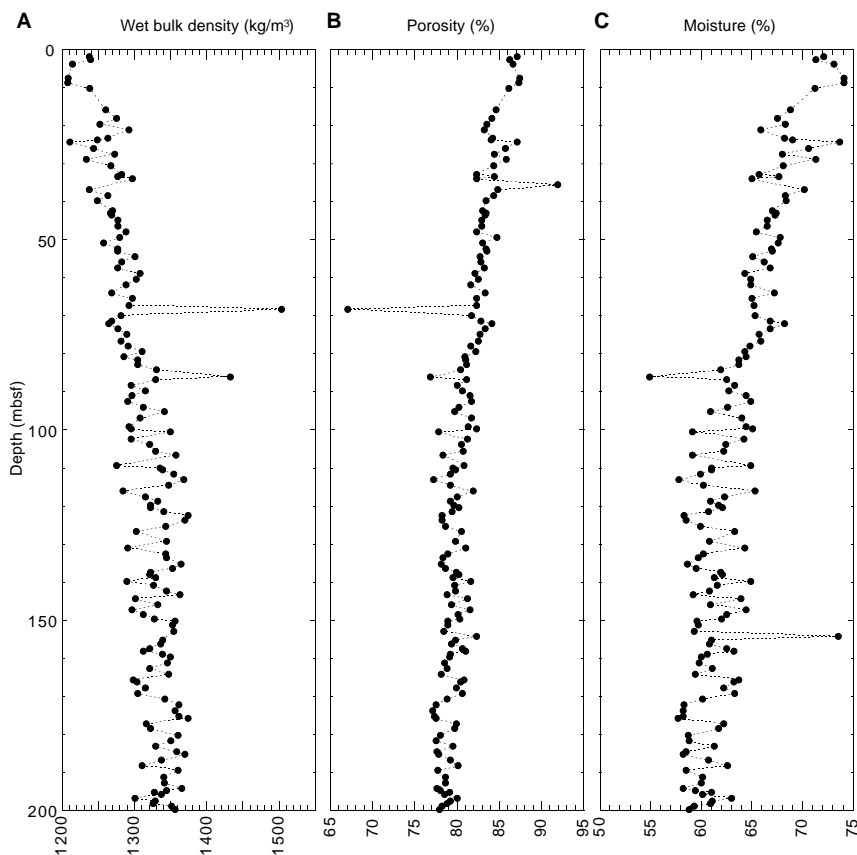


Figure 27. Plots of (A) wet bulk density, (B) porosity, and (C) moisture content derived from index properties measurements at Hole 1077A.

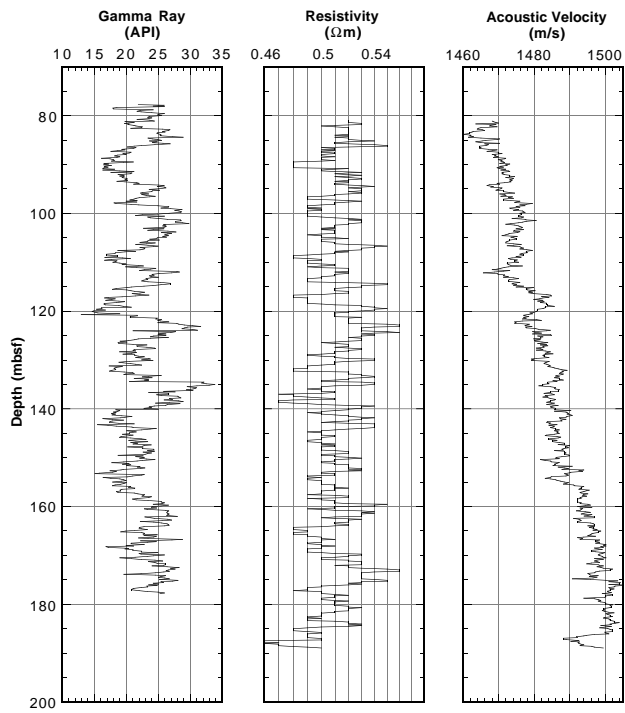


Figure 28. Downhole logs of natural gamma-ray, resistivity, and acoustic velocity for Hole 1077A.

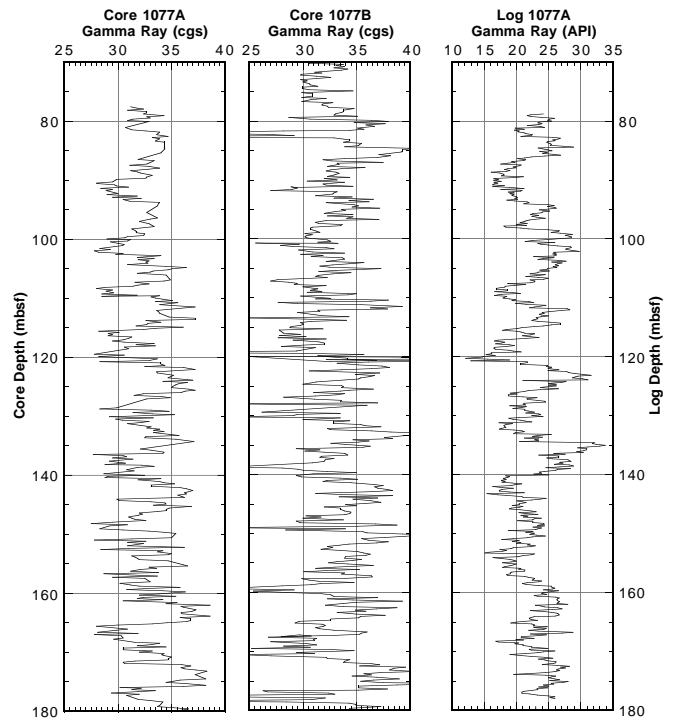


Figure 30. Comparison of core (MST; in centimeter-gram-seconds [cgs]) and log natural gamma-ray data for Holes 1077A and 1077B in the lower part of the logged interval (open hole).

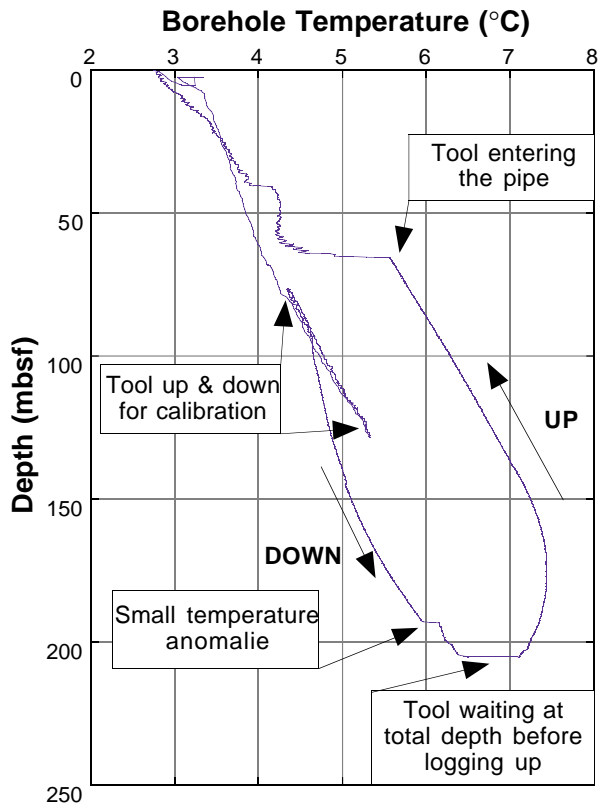


Figure 29. Borehole temperature measurements at Hole 1077A.